MOLECULAR PHYSICS, 1983, VOL. 49, NO. 3, 503–541

Molecular dynamics study of the dynamical properties of an assembly of infinitely thin hard rods

by D. FRENKEL
Fysisch Laboratorium Rijksuniversiteit Utrecht,
P.O. Box 80 000, 3508 TA Utrecht, The Netherlands
and J. F. MAGUIRE
Lear Fan Ltd., 62 Church Road, Newtownabbey, Co. Antrim,
BT36 7LN, Northern Ireland.

(*Received* 19 *November* 1982 ; *accepted* 17 *January* 1983)

We present molecular dynamics (MD) simulations of a system of N ($N=100$–500) infinitely thin hard rods of length L (' hard needles '). An algorithm is described which is reasonably fast and yet is guaranteed not to overlook *any* collision. Under the assumption that successive binary collisions are uncorrelated (the ' Enskog ' assumption), we derive expressions for the time correlation functions of linear and angular momentum and rotational energy. We also obtain an exact expression for the collision frequency in a hard needle fluid. The MD results indicate that the Enskog approach works well at reduced densities below $\rho^*=8$. At higher densities ($8<\rho^*<48$) large deviations from the Enskog predictions are observed. However, at these densities the MD data conform to scaling predictions of the kind first put forward by Doi and Edwards. In particular, we find that the rotational diffusion constant D_R scales as ρ^{*-2}. One of the surprising consequences of the scaling arguments is that the longitudinal self-diffusion coefficient is predicted to diverge as $\rho^* \to \infty$. Such behaviour is indeed observed. Preliminary results on the dynamic orientational correlation factor of the hard needle fluid are presented.

1. INTRODUCTION

Much of our current understanding of dense fluids derives from computer simulations on model systems. Often such calculations provide the only unambiguous test of theoretical predictions concerning the structure and dynamics of dense systems on a microscopic scale. Among the systems studied, the hard sphere fluid (hard disc fluid in 2-D) has played a special rôle. The reason is twofold : computer simulations of the hard sphere fluid could be used to test existing theories of the liquid state, such as the Percus–Yevick equation (equilibrium properties) and the Enskog expressions for transport properties. Such tests, and the discrepancies which they revealed (e.g. Alder and Wainwright's test of the Enskog theory [1]) form the starting point for many of the modern theories of dense fluids. A second reason why the study of the hard sphere fluid has been of special significance is that, once its properties were known, it could serve as a reference system for fluids with continuous intermolecular potentials. This approach has resulted in very successful perturbation theories for dense fluids [2, 3].

In view of the important rôle that the hard sphere system has played, it is somewhat surprising that virtually no work has been reported on other ' one parameter ' hard core systems. We use the term ' one parameter system ' to refer to a model system in which the thermodynamic properties depend on a single parameter. For one-parameter hard core systems, the relevant variable is the reduced density $\rho^* \equiv (N/V)\sigma^3$, where N/V is the number density and σ is a length characteristic of the size of the particle. In three dimensions there are three such one parameter hard core systems : (1) Hard spheres (diameter σ), (2) hard platelets (infinitely thin disks with diameter σ) and (3) hard ' lines ' (infinitely thin needles with length $L=\sigma$). In two dimensions there are two one-parameter hard core systems, viz. hard discs and 2-D hard lines. All of these hard core systems are interesting in their own right : hard spheres (2-D hard discs) serve as a reference system for 3-D (2-D) simple fluids. A system consisting of 3-D hard platelets is a prototype of a (nematic) liquid-crystal-forming fluid [4, 5]. Two dimensional hard lines will form a 2-D liquid crystal at sufficiently high densities [6]. The last of the hard core systems, the 3-D hard lines fluid, appears at first sight to be quite uninteresting because this system has zero excluded volume. As a consequence, the configurational part of the partition function of N hard lines in volume V is of the form :

$$Q_N(V) = (4\pi V)^N/(2^N N!). \tag{1}$$

Hence *all static properties of the hard line system are those of an ideal gas.* This implies that : (*a*) this system has no phase transitions, and (*b*) there are no static correlations, i.e. the pair distribution function is of the form $g(\mathbf{r}_{12}, \boldsymbol{\Omega}_1, \boldsymbol{\Omega}_2) = (4\pi)^{-2}$, where $\mathbf{r}_{12}$ is the distance of molecules 1 and 2, and $\boldsymbol{\Omega}_1$ and $\boldsymbol{\Omega}_2$ their respective orientations. In contrast, all transport properties of this system are strongly density dependent, and this density dependence is non-trivial. It is for this reason that the hard line fluid is ideally suited to test theories of transport phenomena in fluids consisting of highly anisometric molecules. In fact, our interest in the hard line system derives from an experimental study of the rotational dynamics of long rigid viruses in semidilute solution [7–9]. The aim of this experimental study was to test predictions made by Doi and Edwards [10, 11] concerning the density dependence and molecular length dependence of rotational diffusion of rigid linear macromolecules in solution. These predictions, which were based on a scaling approach (see also § 3, below), were corroborated, on most counts, by the light scattering and electric birefringence experiments [7–9]. It was, however, not clear whether the remaining discrepancies between theory and experiment were due to deficiencies in the Doi and Edwards model, or to the fact that real viruses are neither infinitely thin, nor completely rigid. This motivated us to attempt numerical simulation of a simple model system in which scaling behaviour could, presumably, be observed. We were thus led to study the molecular dynamics of a fluid consisting of infinitely thin smooth hard needles. However two points should be stressed. First, the hard line fluid is not really a model for a solution of rigid linear macromolecules because the dynamics in the former system is newtonian rather than brownian, and this has implications for the scaling predictions (see § 3). Secondly, we do not limit our study of the transport properties of the hard line fluid to the scaling regime. In fact, because of its simple structural properties, it is an ideal system to test kinetic theories for transport in molecular fluids.

In a previous publication [12] we reported preliminary results of a molecular dynamics (MD) study of a system of hard needles over a range of densities. In what follows we will use the terms ' hard needles ' and ' hard lines ' interchangeably. Neither term is fully satisfactory ; ' hard needles ' incorrectly suggests a finite thickness, whereas the term ' hard lines ' does not convey the information that the length of the particles under consideration is, in fact, finite. The present paper contains a more detailed, and more up to date, account of our study of the dynamical properties of the hard line fluid. The aim of this paper is threefold : (1) To discuss the computational method used in the simulation, (2) to derive expressions for a number of transport properties of the hard needle system, using two quite different theoretical approaches, viz. kinetic theory and the, appropriately modified, scaling method of Doi and Edwards, and (3) to compare the numerical results with the theoretical predictions. The three topics mentioned above will be dealt with in separate, and largely independent, sections. Readers who are not interested in the computational method or the theoretical background can skip the relevant sections.

2. Computational method

2.1. *General aspects*

To our knowledge, there has been relatively little work done on the dynamics of anisometric molecules with impulsive interactions. The dynamics of 256 hard spherocylinders has been studied by Rebertus and Sando [13]. The algorithm used by these authors was rather time consuming, particularly at high densities, and hence the simulations were limited to two thermodynamic state points. Moreover, the computational method used in [13] will overlook a small but finite number of collisions. Bellemans and co-workers [14] have reported the simulation of a two dimensional system consisting of 32 dimers of hard discs. The study was limited to one thermodynamic state, and few details are given. Computational techniques to simulate the dynamics of non-spherical molecules undergoing (among other forces) impulsive interactions have been proposed in a paper by Stratt, Holmgren and Chandler [15] and, more recently, in a paper by McNeil and Madden [16]. The former article indicates how to deal with holonomic constraints in the presence of impulsive forces. Both the work of Rebertus and Sando and the work of Stratt *et al.* rely on the fact that hard core overlaps can be detected *a posteriori* and yet be dealt with satisfactorily. This approach is developed and systematically tested in the paper by McNeil and Madden. The fact that so few computational results on the dynamics of anisometric hard core systems have been published, suggests that the computational methods that have been developed to simulate hard sphere systems cannot be readily generalized to handle non-spherical particles. The problem is that whereas for hard spheres it is computationally easy to decide if and when two particles are going to collide, for non-spherical molecules such a criterion, although not necessarily hard to formulate, may be time consuming to test. The strategy advocated in [13, 15, 16] is based on the fact that it is often easier to detect if two particles are in fact overlapping, and then work back to the instant of the impulsive collision. This approach does not work for the hard line fluid because, as the particles are infinitely thin, they never overlap, even if they have just collided. So for this particular case there is really no way around an

a priori search for the time of the next collision. However, as it will turn out, this direct method is not necessarily prohibitively time consuming and it is therefore conceivable that the methods employed in the present work could, in some cases, compete with techniques based on *a posteriori* overlap detection. The present method is certainly to be preferred in situations where it is essential that no collisions are overlooked.

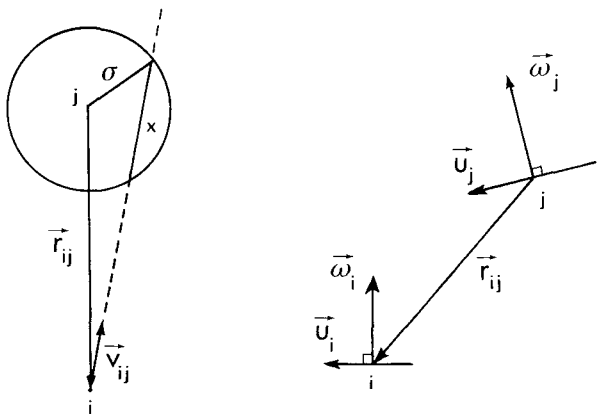

Figure 1. Left: Geometrical construction to determine if and when 2 hard spheres i and j with relative distance $\mathbf{r}_{ij}$ and relative velocity $\mathbf{v}_{ij}$ are going to collide. The condition $\delta^2>0$ (2 *b*) is equivalent to $x^2>0$ (see drawing) because $4\delta^2=x^2 v_{ij}^2$. Right: Schematic drawing of two hard needles i and j at distance $\mathbf{r}_{ij}$. The molecular orientations $\mathbf{u}_{i(j)}$ are perpendicular to the angular velocities $\boldsymbol{\omega}_{i,(j)}$. A collision can only occur if $\mathbf{u}_i$, $\mathbf{u}_j$ and $\mathbf{r}_{ij}$ are all in one plane (4).

To illustrate the complications that arise in searching for the next collision of two non-spherical molecules, we will compare the test that is needed to determine whether two hard needles of length L are about to collide, with the corresponding test for hard spheres. Two hard spheres i and j of diameter σ, with relative velocity $\mathbf{v}_{ij}=\mathbf{v}_i-\mathbf{v}_j$ and interatomic distance $\mathbf{r}_{ij}(t)=\mathbf{r}_i(t)-\mathbf{r}_j(t)$ will collide if the following conditions are satisfied [17, 18] (see figure 1):

$$\mathbf{r}_{ij}(t)\,.\,\mathbf{v}_{ij}<0, \tag{2 a}$$

$$\delta^2\equiv v_{ij}^2(\sigma^2-r_{ij}^2(t))+(\mathbf{r}_{ij}(t)\,.\,\mathbf{v}_{ij})^2>0. \tag{2 b}$$

If $\delta^2>0$, then the time of the next collision between i and j (disregarding all other particles, for the moment) is given by

$$t_c=t-(\mathbf{r}_{ij}(t)\,.\,\mathbf{v}_{ij}+\delta)/v_{ij}^2. \tag{2 c}$$

Clearly, knowledge of $\mathbf{r}_{ij}$ and $\mathbf{v}_{ij}$ at time t is all that is needed to evaluate δ, and hence t_c. Let us now consider the case of two hard needles i and j of length L, with relative velocity $\mathbf{v}_{ij}$, angular velocities $\boldsymbol{\omega}_i$ and $\boldsymbol{\omega}_j$, orientation unit vectors $\mathbf{u}_i(t)$ and $\mathbf{u}_j(t)$, and centre of mass distance $\mathbf{r}_{ij}(t)$ (figure 1). The criterion that must be satisfied at the time of a collision is

$$\mathbf{r}_{ij}(t_c)+\alpha\mathbf{u}_i(t_c)-\beta\mathbf{u}_j(t_c)=0 \tag{3 a}$$

with:

$$|\alpha|<L/2 \quad \text{and} \quad |\beta|<L/2. \tag{3 b}$$

These conditions can be rewritten in the following form :

$$f(t_c) \equiv \mathbf{u}_i(t_c) \wedge \mathbf{u}_j(t_c) \cdot \mathbf{r}_{ij}(t_c) = 0, \tag{4}$$

$$\left.\begin{aligned} \alpha &= -(\mathbf{r}_{ij}(t_c) \cdot \mathbf{u}_i(t_c) - (\mathbf{r}_{ij}(t_c) \cdot \mathbf{u}_j(t_c))(\mathbf{u}_i(t_c) \cdot \mathbf{u}_j(t_c)))/(1-(\mathbf{u}_i(t_c) \cdot \mathbf{u}_j(t_c))^2), \\ \beta &= -(\mathbf{r}_{ij}(t_c) \cdot \mathbf{u}_j(t_c) - (\mathbf{r}_{ij}(t_c) \cdot \mathbf{u}_i(t_c))(\mathbf{u}_i(t_c) \cdot \mathbf{u}_j(t_c)))/(1-(\mathbf{u}_i(t_c) \cdot \mathbf{u}_j(t_c))^2) \end{aligned}\right\} \tag{5}$$

and

$$|\alpha| < L/2, \quad |\beta| < L/2. \tag{6}$$

In general, there will be many values of t_c for which (4) is satisfied. The desired collision time is the smallest value of t_c ($> t$) for which the subsidiary conditions (6) are fulfilled. In contrast to the hard sphere case, the roots of (4) can only be determined numerically. Accepting this fact, we will have to look for an algorithm that solves (4) by brute force, yet at the same time, is written in such a way that the number of times that (4) has to be solved is minimal. It is perhaps worth pointing out that the method advocated in [13, 15, 16] is certainly optimal in this sense : one only starts solving the equivalent of (4) ' when it is too late '. As explained above, we cannot employ this method. Below, we describe an algorithm to solve (4) *a priori*. We have found this algorithm to be quite efficient, but we do not claim that it is unique or optimal ; there is probably room for substantial improvement.

The root-searching routine consists of two parts : in the first part a number of simple tests are carried out to put upper and lower bounds on the time of the next collision of particles i and j. Most collision candidates will be rejected by these tests. If, however, there remains a finite interval $t_{low} < t < t_{up}$ in which one or more collisions could occur, then the second part of the routine will systematically search for the smallest root of (4) that satisfies the subsidiary conditions (6). This part may be time consuming because there may be several acceptable roots in the interval $\{t_{low}, t_{up}\}$ and it is crucial to locate the lowest such root. In the next two sub-sections we describe the procedure to find the next collision (if any) of particles i and j. After that, we indicate how the root-searching routine fits into the main program. Finally we discuss the collision dynamics of two hard needles.

2.2. *Upper and lower bounds on* t_c

Suppose that we wish to find the first collision of a particle i with any particle $j \neq i$, given all particle coordinates and momenta (both linear and angular) at time $t = t_0$. Clearly, our initial, and most conservative estimate of t_{low} is : $t_{low} = t_0$. We can also put an initial upper bound on t_c. This upper bound derives from the fact that we employ periodic boundary conditions, and that we wish to find the first collision of i with *the nearest image* of j. As both i and j move, the nearest image of j may change with time. To give a specific example, suppose that particles i and j are initially separated by $r_{ij} = (x_{ij}, 0, 0)$, with $|x_{ij}| < D/2$ (D stands for the diameter of the periodic box which, for convenience, we have chosen to be cubic). The distance $x'_{ij} = D - |x_{ij}| > D/2$. As particles i and j move apart, $|x'_{ij}|$ will decrease ; first it will become smaller than $D/2$ and eventually : $|x'_{ij}(t)| < L$. From that moment on a collision between i and

what used to be the next nearest image of j may take place. For this to happen, the relative distance of i and j must have changed by at least $D/2-L$. Hence either i or j (or both) must have moved over a distance greater than $(D/2-L)/2$ in the + or − x-direction. The time this takes (e.g. for particle i) is given by

$$t_i^x = (D/2-L)/(2|v_x|^i). \tag{7}$$

In the general case, similar expressions for t_i^y and t_i^z will result. We define a time $t_i^{\max}$ by

$$t_i^{\max} = \text{Min}\,(t_i^x, t_i^y, t_i^z). \tag{8}$$

Clearly, after a time $t_i^{\max}$ ($t_j^{\max}$) the information on possible collision partners of i (j) will have to be updated anyway. Therefore we initially set the upper limit of the interval within which we search for collisions of particle i equal to

$$t_{\text{up}} = t_0 + t_i^{\max}. \tag{9}$$

If, as sometimes happens, particle i survives during this interval without suffering collisions, we initiate a new search for collision partners of particle i at time t_{up}. As the same procedure is followed for particle j, there is no chance that we will overlook collisions of i with any periodic image of j.

Having fixed the initial upper and lower limits of the interval in which we are to search for collisions, we will now attempt to narrow these bounds. If we had already located the time of collision of particle i with another particle k, then this time ($t_c(k)$) can serve as an improved upper limit : $t_{\text{up}} = t_c(k)$. In this way we guarantee that we only search for the very first collision of i. Next we perform three tests that are related to the simple fact that, in order to have a collision, needles i and j must be close enough to touch. The first criterion simply states that, in order to touch, two needles i and j should be within a distance L from one another :

$$(\mathbf{r}_{ij}(t_0) + \mathbf{v}_{ij}\Delta t)^2 < L^2. \tag{10}$$

This expression, which is identical to the hard sphere criterion (2 b), puts an upper and lower bound on $\Delta t = t_c - t_0$:

$$\Delta t = (-\mathbf{r}_{ij}(t_0) \,.\, \mathbf{v}_{ij} \pm ((L^2 - r_{ij}^2(t_0))v_{ij}^2 + (\mathbf{r}_{ij}(t_0) \,.\, \mathbf{v}_{ij})^2)^{1/2})/v_{ij}^2. \tag{11}$$

If this new upper (lower) bound is smaller (larger) than the original one, the latter is replaced by the former. If there is no Δt for which (10) is satisfied, particle j is rejected as a possible collision partner of i. It is worth noting that this does not exclude the possibility that i will later collide with another periodic image of j. The following two tests state that, in order for particles i and j to collide the disc swept out by needle i as it rotates in a plane perpendicular to its (fixed) angular momentum $\mathbf{J}_i$ must intersect the plane in which j rotates, and *vice versa*. This leads to the conditions (see figure 2)

$$(L/2)^2(1-(\mathbf{j}_i \,.\, \mathbf{j}_j)^2) > (\mathbf{r}_{ij}(t) \,.\, \mathbf{j}_i)^2 \tag{12 a}$$

and

$$(L/2)^2(1-(\mathbf{j}_i \,.\, \mathbf{j}_j)^2) > (\mathbf{r}_{ij}(t) \,.\, \mathbf{j}_j)^2, \tag{12 b}$$

where $\mathbf{j}_i$ ($\mathbf{j}_j$) is a unit vector in the direction of $\mathbf{J}_i$ ($\mathbf{J}_j$). Both (12 a) and (12 b) may lead to improved upper (lower) bounds on the collision interval. If either (12 a) or (12 b) is never satisfied, particle j cannot collide with i within the previously specified interval. The bounds on the interval to be searched that

follow from (12 *a*) are

$$\Delta t = (-(\mathbf{r}_{ij}(t_0) \cdot \mathbf{j}_i) \pm \frac{L}{2}(1-(\mathbf{j}_i \cdot \mathbf{j}_j)^2)^{1/2})/(v_{ij} \cdot \mathbf{j}_i). \tag{13}$$

A similar expression follows from (12 *b*). If the above tests have failed to exclude collisions between particles i and j, we proceed to search for roots of (4) in the interval $\{t_{\text{low}}, t_{\text{up}}\}$.

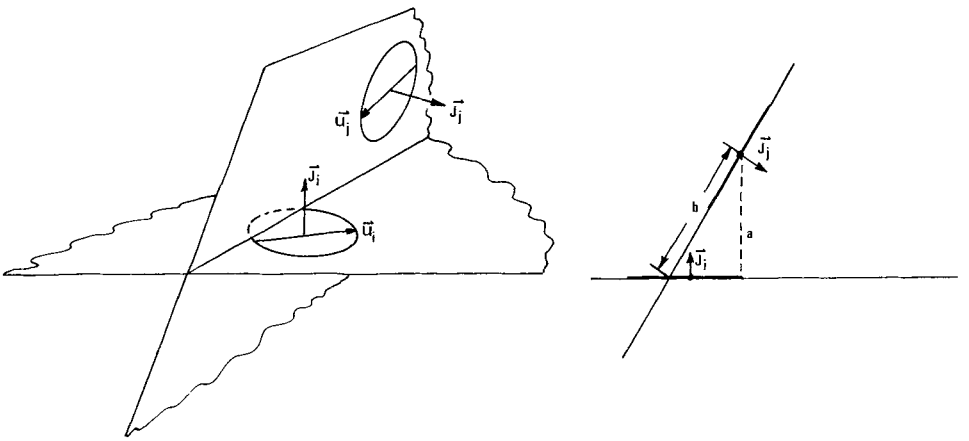

Figure 2. A necessary (but not sufficient) condition for a collision between two lines of length L is that a disc of diameter L perpendicular to the angular momentum of molecule i intersects a corresponding disc through molecule j. The right hand figure is obtained by projecting the left hand drawing onto a plane parallel to both $\mathbf{J}_i$ and $\mathbf{J}_j$. The condition in (12 *a*) is equivalent to the condition $L/2 > b$. Note that 'a' in the figure equals $|\mathbf{r}_{ij} \cdot \mathbf{j}_i|$.

2.3. *Search for collisions*

Finding acceptable roots of (4) is not particularly difficult. It is, however, less than trivial to make sure that no collisions are overlooked. To eliminate the possibility that acceptable roots are missed, we follow a root-searching procedure which, once a root of (4) has been located, continues to search for earlier roots (if any). As this search proceeds, the upper and lower bounds on the interval in which such earlier collisions might take place are continuously improved until either a root is found, or the lower bound becomes larger than the upper bound. In the latter case, the possibility of any earlier roots has been positively eliminated. In deriving such improved upper and lower bounds, we make use of the fact that, once we know the coordinates and (angular) momenta of the potential collision partners at a given time t, we can compute a lower bound on the size of the interval around time t during which collisions between i and j are rigorously excluded. To this end, we first evaluate upper bounds to the absolute values of the first and second derivatives of the function $f_{ij}(t) = \mathbf{u}_i(t) \wedge \mathbf{u}_j(t) \cdot \mathbf{r}_{ij}(t)$ (cf. (4)). The first time derivative of $f_{ij}(t)$ is given by

$$\dot{f}_{ij}(t) = (\mathbf{u}_i(t) \cdot \mathbf{r}_{ij}(t))(\Delta\boldsymbol{\omega}_{ij} \cdot \mathbf{u}_j(t)) + (\mathbf{u}_j(t) \cdot \mathbf{r}_{ij}(t))(\Delta\boldsymbol{\omega}_{ij} \cdot \mathbf{u}_i(t)) - (\Delta\boldsymbol{\omega}_{ij} \cdot \mathbf{r}_{ij}(t))(\mathbf{u}_i(t) \cdot \mathbf{u}_j(t)) + \mathbf{u}_i(t) \wedge \mathbf{u}_j(t) \cdot \mathbf{v}_{ij}, \tag{14}$$

where $\Delta\boldsymbol{\omega}_{ij}=\boldsymbol{\omega}_i-\boldsymbol{\omega}_j$. Similarly, the expression for the second time derivative of $\dot{f}_{ij}(t)$ is given by

$$\begin{aligned}\ddot{f}_{ij}(t)=2\{&(\mathbf{u}_i(t)\cdot\mathbf{v}_{ij})(\Delta\boldsymbol{\omega}_{ij}\cdot\mathbf{u}_j(t))+(\mathbf{u}_j(t)\cdot\mathbf{v}_{ij})(\Delta\boldsymbol{\omega}_{ij}\cdot\mathbf{u}_i(t))\\&-(\mathbf{u}_i(t)\cdot\mathbf{u}_j(t))(\Delta\boldsymbol{\omega}_{ij}\cdot\mathbf{v}_{ij})\}-(\Delta\boldsymbol{\omega}_{ij}\cdot\mathbf{r}_{ij}(t))(\Delta\boldsymbol{\omega}_{ij}\cdot\mathbf{u}_i(t)\wedge\mathbf{u}_j(t))\\&+(\mathbf{u}_i(t)\cdot\mathbf{r}_{ij}(t))(\mathbf{u}_j(t)\cdot\boldsymbol{\omega}_i\wedge\boldsymbol{\omega}_j)+(\mathbf{u}_j(t)\cdot\mathbf{r}_{ij}(t))(\mathbf{u}_i(t)\cdot\boldsymbol{\omega}_i\wedge\boldsymbol{\omega}_j)\\&+(\Delta\boldsymbol{\omega}_{ij}\cdot\mathbf{u}_i(t))(\mathbf{r}_{ij}(t)\cdot\boldsymbol{\omega}_j\wedge\mathbf{u}_j(t))+(\Delta\boldsymbol{\omega}_{ij}\cdot\mathbf{u}_j(t))(\mathbf{r}_{ij}(t)\cdot\boldsymbol{\omega}_i\wedge\mathbf{u}_i(t)).\end{aligned}\tag{15}$$

An upper bound to $\dot{f}_{ij}(t)$ (14) can be found by noting that (14) is of the form

$$\dot{f}_{ij}(t)=\mathbf{r}_{ij}(t)\cdot\mathbf{M}(t)\cdot\Delta\boldsymbol{\omega}_{ij}+\mathbf{u}_i(t)\wedge\mathbf{u}_j(t)\cdot\mathbf{v}_{ij},\tag{16}$$

where the matrix $\mathbf{M}$ is given by

$$\mathbf{M}=\mathbf{u}_i\mathbf{u}_j+\mathbf{u}_j\mathbf{u}_i-(\mathbf{u}_i\cdot\mathbf{u}_j)\mathbf{I}.\tag{17}$$

In the above equation, $\mathbf{I}$ stands for the unit matrix. It is easy to show that the eigenvalues of $\mathbf{M}$ are : $+1$, -1 and $-(\mathbf{u}_i\cdot\mathbf{u}_j)$. Hence no eigenvalue of $\mathbf{M}$ has an absolute value larger than 1. It then follows that :

$$|\dot{f}_{ij}(t)|\leqslant|\mathbf{r}_{ij}(t)|\cdot|\Delta\boldsymbol{\omega}_{ij}|+|\mathbf{v}_{ij}|.\tag{18}$$

If we denote the maximum value of $|\mathbf{r}_{ij}(t)|$ in the interval $\{t_{\text{low}},\ t_{\text{up}}\}$ by $r_{ij}{}^m$, we obtain the following absolute upper bound on $\dot{f}_{ij}(t)$ in the interval $\{t_{\text{low}},\ t_{\text{up}}\}$:

$$|\dot{f}_{ij}(t)|\leqslant\dot{f}_{ij}{}^m\equiv r_{ij}{}^m\cdot|\Delta\boldsymbol{\omega}_{ij}|+|\mathbf{v}_{ij}|.\tag{19}$$

Similarly, it can be shown that the absolute value of $\ddot{f}_{ij}(t)$ in the interval $\{t_{\text{low}},\ t_{\text{up}}\}$ must be smaller than $\ddot{f}_{ij}{}^m$, given by :

$$\ddot{f}_{ij}{}^m\equiv|\Delta\boldsymbol{\omega}_{ij}|\cdot\{2|\mathbf{v}_{ij}|+r_{ij}{}^m(|\boldsymbol{\omega}_i|+|\boldsymbol{\omega}_j|)\}.\tag{20}$$

Equations (14) and (15) are the central equations in our root-searching procedure, while (20) will be used to obtain improved bounds on the interval within which collisions may occur. As we shall now proceed to show, the procedure that we employ is guaranteed to locate the earliest acceptable root in the interval $\{t_{\text{low}},\ t_{\text{up}}\}$.

Consider a situation where $f_{ij}(t)$ behaves as shown in figure 3. We assume that $f_{ij}(t)$ has three roots in the interval $\{t_{\text{low}},\ t_{\text{up}}\}$, two of which, say t_1 and t_3, satisfy condition 6 ; the desired root, in this case would, of course, be t_1. We start by computing f_{ij}, $\dot{f}_{ij}$ and $\ddot{f}_{ij}$ at $t=t_{\text{low}}$. Using the values thus obtained, we arrive at a first estimate of the root by solving for the smallest positive root (if any) of the quadratic equation

$$f_{ij}+\dot{f}_{ij}\Delta t+\tfrac{1}{2}\ddot{f}_{ij}\Delta t^2=0.\tag{21}$$

At the same time we improve our estimate of the lower bound, t_{low}, by solving for the smallest positive root of :

$$f_{ij}+\dot{f}_{ij}\Delta t'\pm\tfrac{1}{2}\ddot{f}_{ij}{}^m\,\Delta t'^2=0\tag{22}$$

(see the dashed parabola in Figure 3). The $+$ $(-)$ sign in (22) applies when f_{ij} is negative (positive). In case (21) has no positive roots, we restart the procedure from the new t_{low} :

$$t_{\text{low}}{}^{\text{new}}=t_{\text{low}}{}^{\text{old}}+\Delta t'.\tag{23}$$

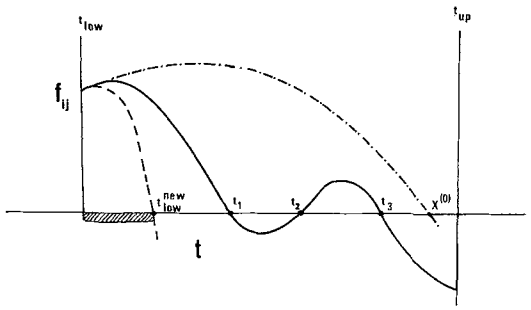

Figure 3. Typical example of the time dependence of the function $f_{ij}(t)$ defined above (14). In this drawing the functions $f_{ij}(t)$ has 3 roots in the interval $\{t_{\text{low}}, t_{\text{up}}\}$. An improved estimate of t_{low}, $t_{\text{low}}{}^{\text{new}}$ is obtained from (22). A first estimate of the desired root is found by solving (21) (dash-dot parabola) yielding $x^{(0)}$. An improved estimate $x^{(1)}$ (not shown) is obtained by solving (21) at $x^{(0)}$, and so on.

In what follows t_{low} always refers to the most recent value of $t_{\text{low}}{}^{\text{new}}$. If the root, estimated from (21) is larger than t_{up} we restart our search from t_{up} (thereby obtaining an improved estimate of t_{up} from the smallest (in absolute sense) negative root of (22), evaluated at t_{up}). Suppose, however, that our initial estimate of the root is at $x^{(0)}$ (see figure 3). The root-searching routine will now iterate and find successive estimates $x^{(1)}$, $x^{(2)}$, etc., which will rapidly converge to t_3. Having found this root, the routine tests the subsidiary conditions (6), and concludes that t_3 is indeed an acceptable root. But, of course, there can still be additional roots in the interval $\{t_{\text{low}}, t_3\}$. Actually, we can narrow this interval down somewhat by observing that there can be no roots between t_3 and $t_3 - 2|\dot{f}_{ij}(t_3)|/\ddot{f}_{ij}{}^m \equiv t'_{\text{up}}$. So next we have to search for roots in the interval $\{t_{\text{low}}, t'_{\text{up}}\}$, following the procedure described above. Suppose that we have the bad luck to find root t_2 first (in practice this is extremely unlikely, as the search always restarts from t_{low}). This root will be rejected because it does not satisfy the subsidiary conditions (6). The search for earlier roots therefore continues (to be more precise, it would have continued anyway, as long as there is a finite open interval between the current root and t_{low} left). We now have to search for roots in the interval $\{t_{\text{low}}, t''_{\text{up}}\}$, where $t''_{\text{up}} = t_2 - 2|\dot{f}_{ij}(t_2)|/\ddot{f}_{ij}{}^m$. During this search the root t_1 will be found. It is clear that this procedure will work, irrespective of the number of roots in the interval $\{t_{\text{low}}, t_{\text{up}}\}$. Let us finally consider the possible situation that t_1 is *not* an acceptable root ; in that case t_3 would be the desired root. Of course, we had already located this root previously and so it would seem obvious that information about this root has been stored and can now be retrieved. Actually, this kind of bookkeeping greatly complicates the program, and we found it preferable to simply restart the root-searching procedure in the new interval t_{low}, t_{up}, where the new value of t_{low} is given by $t_{\text{low}} = t_1 + 2|\dot{f}_{ij}(t_1)|/\ddot{f}_{ij}{}^m$. Inefficient though this approach may seem, it does not cost much additional time (because the scenario described above is not very common), yet it greatly simplifies the structure of the root-searching routine. A very schematic representation of this structure is shown in figure 4. It might seem that a considerable simplification of the program could be achieved by using the normal linear Newton–Raphson root-searching method, rather than the

quadratic one described above. We have tested the linear method and found it unsatisfactory because, apart from being somewhat slower than the quadratic method, it sometimes ran into problems of poor convergence.

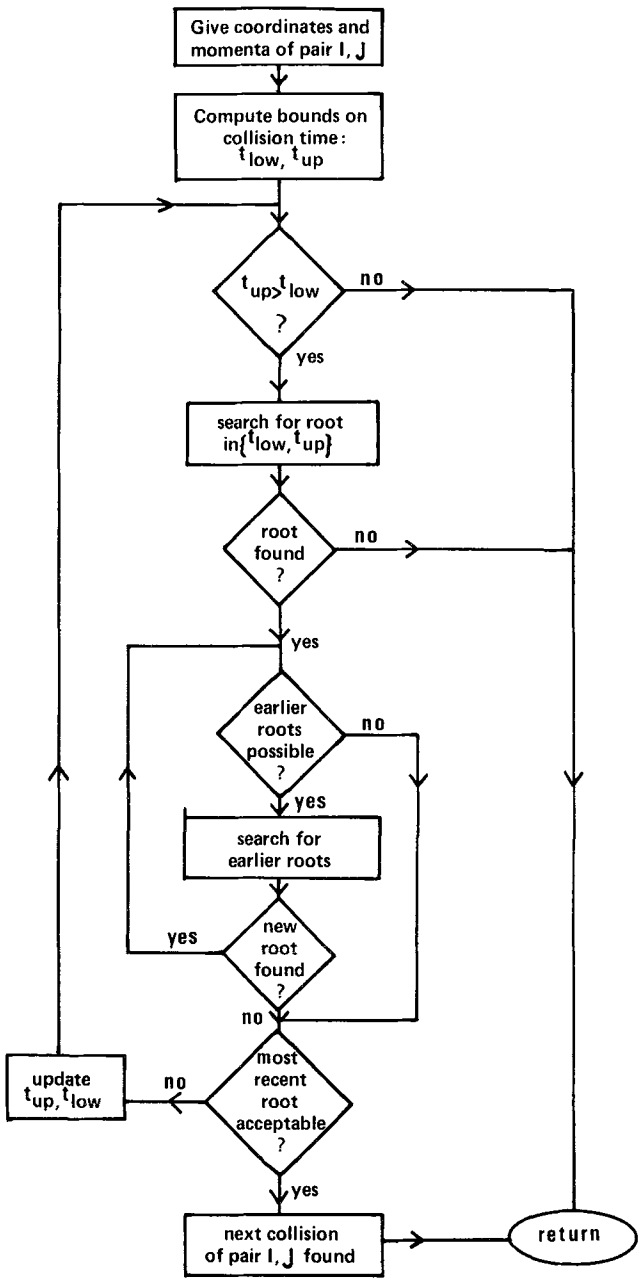

Figure 4. Schematic representation of the central part of the root-searching routine described in the text.

Finally, in this section on the root-searching procedure, we should mention a special kind of collision that can occur in the system under consideration or, for that matter, in any fluid of anisometric molecules, but not in a hard sphere fluid. If, in a hard sphere fluid two particles i and j collide, then either i or j or both must collide with at least one other particle before i and j can recollide. This is no longer true for hard needles ; here the possibility exists that i and j recollide without any intervening collisions with a third particle. In order to find the next collision of i and j we have to search for the first (acceptable) root of (4). But in this particular case all our previous estimates of t_{low} will yield $t_{\text{low}}=t_0$, with $f_{ij}(t_0)=0$. Clearly, there is a risk that our root-searching routine will immediately find an apparently acceptable root at $t=t_0$. To eliminate this possibility, we compute $\dot{f}_{ij}(t_0+\epsilon)$ and $\dot{f}_{ij}{}^{m}(t_0+\epsilon)$, where $t_0+\epsilon$ denotes a time immediately after the most recent collision of particles i and j. No recollision of i and j is possible before a time $t_{\text{low}}=t_0+2|\dot{f}_{ij}(t_0+\epsilon)|/|\dot{f}_{ij}{}^{m}(t_0+\epsilon)$. Using this value of t_{low}, the search for collisions between particles i and j proceeds as before.

2.4. *Equilibration and collision dynamics*

From the discussion above it is obvious that the procedure to find the time of the next collision between two hard lines is quite different from the corresponding part of the usual hard sphere MD programme. For the rest, however, the hard line and hard sphere programmes are in essence the same. Excellent reviews on the practical aspects of MD simulation of hard sphere fluids exist, to which we refer the reader for details [18]. Here we shall discuss only those sections of the hard line MD programme that are different from the corresponding part of a hard sphere programme. Clearly, the routine that handles the dynamics of a collision between two hard needles belongs to this category. The special properties of the hard needle fluid are also exploited in the routine that generates fully equilibrated initial configurations for the MD runs. Both routines are discussed below.

In the usual MD simulation the generation of a sufficiently equilibrated initial configuration may be rather time consuming. Often as much as 10–20 per cent of the total computing time is spent on equilibration runs. Fortunately, the hard line fluid can be prepared directly in a fully equilibrated configuration, because the static properties of the hard line fluid are those of an ideal gas (see (1)). It therefore suffices to distribute the centres of mass of the needles randomly over the periodic box, while the molecular orientation vectors are distributed isotropically over the surface of a sphere. At the same time, the molecular velocities, and angular velocities, are chosen at random from the appropriate Maxwell–Boltzmann distribution. The configuration thus generated has all the properties of a fully equilibrated hard line fluid.

The dynamics of a collision between two hard needles depends on the coordinates and (angular) momenta of the colliding particles. During the collision energy, angular momentum and linear momentum must be conserved. We assume that during the collision an impulsive force, perpendicular to both needles, acts at the point of contact (N.B. for ' rough ' hard lines the impulsive force need not be perpendicular to the needles). In the present work we have assumed that mass is distributed uniformly over the length of the needles ; this implies that the moment of inertia of a needle is given by : $I=mL^2/12$. Of

course, these assumptions are in no way essential to the working of the programme ; the modifications required to simulate the dynamics of *rough* needles with non-uniform mass distribution are trivial.

Let us consider two particles i and j with initial linear and angular momenta $\mathbf{p}_i$, $\mathbf{p}_j$ and $\mathbf{J}_i$, $\mathbf{J}_j$. At the time of collision, particles i and j touch at a point $\mathbf{r}_0$. According to (3), $\mathbf{r}_0$ is given by

$$\mathbf{r}_0 = \mathbf{r}_i + \alpha \mathbf{u}_i = \mathbf{r}_j + \beta \mathbf{u}_j. \tag{24}$$

It is convenient to choose a coordinate system with its origin at $\mathbf{r}_0$. In this frame

$$\left.\begin{aligned} \mathbf{r}_i &= -\alpha \mathbf{u}_i \\ \text{and} \qquad \mathbf{r}_j &= -\beta \mathbf{u}_j. \end{aligned}\right\} \tag{24 a}$$

After the collision, both particles have new linear and angular momenta $\mathbf{p}'_i$, $\mathbf{p}'_j$, $\mathbf{J}'_i$ and $\mathbf{J}'_j$. Conservation of linear momentum implies

$$\left.\begin{aligned} \mathbf{p}'_i &= \mathbf{p}_i + \Delta\mathbf{P}, \\ \mathbf{p}'_j &= \mathbf{p}_j - \Delta\mathbf{P}, \end{aligned}\right\} \tag{25}$$

where $\Delta\mathbf{P}$ is the, as yet undetermined, impulsive momentum transfer. By assumption, $\Delta\mathbf{P}$ is perpendicular to both $\mathbf{u}_i$ and $\mathbf{u}_j$. The new angular momenta are given by

$$\left.\begin{aligned} \mathbf{J}'_i &= \mathbf{J}_i + \alpha \mathbf{u}_i \wedge \Delta\mathbf{P}, \\ \mathbf{J}'_j &= \mathbf{J}_j - \beta \mathbf{u}_j \wedge \Delta\mathbf{P}. \end{aligned}\right\} \tag{26}$$

Conservation of total angular momentum is then automatically satisfied :

$$\mathbf{J}_i + \mathbf{J}_j - \alpha \mathbf{u}_i \wedge \mathbf{p}_i - \beta \mathbf{u}_j \wedge \mathbf{p}_j = \mathbf{J}'_i + \mathbf{J}'_j - \alpha \mathbf{u}_i \wedge \mathbf{p}'_i - \beta \mathbf{u}_j \wedge \mathbf{p}'_j. \tag{27}$$

Conservation of energy requires that

$$\begin{aligned} p_i^2/2m + p_j^2/2m + J_i^2/2I + J_j^2/2I = (\mathbf{p}_i + \Delta\mathbf{P})^2/2m + (\mathbf{p}_j - \Delta\mathbf{P})^2/2m \\ + (\mathbf{J}_i + \alpha \mathbf{u}_i \wedge \Delta\mathbf{P})^2/2I + (\mathbf{J}_j - \beta \mathbf{u}_j \wedge \Delta\mathbf{P})^2/2I. \end{aligned} \tag{28}$$

Equation 28 can be rewritten as

$$\Delta\mathbf{P} \cdot ((\mathbf{p}_i - \mathbf{p}_j)/2m + (\alpha \mathbf{J}_i \wedge \mathbf{u}_i - \beta \mathbf{J}_j \wedge \mathbf{u}_j)/I) = -\Delta P^2 (1/m + (\alpha^2 + \beta^2)/2I). \tag{29}$$

It should be noted that the first term between brackets in (29) is just the relative velocity of the needles *at the point of contact* (' $\Delta\mathbf{v}_{\text{imp}}$ '). As $\Delta\mathbf{P}$ is perpendicular to $\mathbf{u}_i$ and $\mathbf{u}_j$, we finally obtain :

$$\Delta\mathbf{P} = -(\Delta\mathbf{v}_{\text{imp}})_\perp / (1/m + (\alpha^2 + \beta^2)/2I), \tag{30}$$

where $(\Delta\mathbf{v}_{\text{imp}})_\perp$ denotes the component of $\Delta\mathbf{v}_{\text{imp}}$ perpendicular to both $\mathbf{u}_i$ and $\mathbf{u}_j$.

3. Transport properties

3.1. *General*

Approximate expressions for some of the transport properties of the hard line fluid can be derived in the limit of low and high densities. In the low density regime we use kinetic theory to arrive at expressions for some of the correlation

functions characterizing translational and rotational diffusion. Our approach is basically the same as the ' Enskog ' method used by Berne and co-workers [19–21] to describe the transport properties of the rough sphere fluid. At high densities ($\rho^* \gg 1$) such an approach, based on the assumption of uncorrelated binary collisions, will fail. It is however precisely at high densities that the scaling theory put forward by Doi and Edwards [10, 11] might provide a valid description of the rotational and translational motion of the needles. In the following two sub-sections we present the appropriate expressions for the rotational and translational diffusion of *smooth* hard needles in the kinetic and scaling regimes. Moreover, we derive an expression for the collision frequency in the hard line fluid that is *exact* at all densities.

3.2. *Kinetic regime*

During a collision, the velocity, angular momentum and kinetic energy of a molecule i change abruptly. As a consequence, the initial slope of the correlation function of any of the above variables is non-zero :

$$\lim_{t \to 0+} \langle A(0)A(t)\rangle / \langle A^2(0)\rangle = -1/\tau_A, \tag{31}$$

where A stands for either $\mathbf{v}_i$, $\boldsymbol{\omega}_i$ or $\epsilon_i - \langle \epsilon_i \rangle$. Chandler [22, 23] has shown that, if the effect of correlated binary collisions can be neglected, the correlation function $C_A(t) \equiv \langle A(0)A(t)\rangle / \langle A^2 \rangle$ is completely determined by its initial slope, and has the form :

$$C_A(t) = \exp(-t/\tau_A). \tag{32}$$

Equation (32) corresponds to a truncation of the cumulant expansion of $C_A(t)$ after the first term. This approximation for $C_A(t)$ is often referred to as an ' Enskog ' approximation because it relies on the neglect of correlated binary collisions. For a more detailed discussion of this point, we refer the reader to the relevant publications by Chandler [22, 23] and by O'Dell and Berne [19]. The Enskog approximation is particularly useful in the hard line system because the initial slopes of the type given by (31) can be calculated *exactly* at any density. Consistent with the use of the Enskog approximation for $\langle \mathbf{J}(0) \cdot \mathbf{J}(t)\rangle$, is the use of Gordon's J-diffusion model [24, 25] for the orientational correlation functions $C_l(t) \equiv \langle P_l(\mathbf{u}(0) \cdot \mathbf{u}(t))\rangle$, where $\mathbf{u}(t)$ is the molecular orientation vector at time t, and $P_l(x)$ is the lth Legendre polynomial. The ' collision frequency ' $\beta^{J\text{-diff.}}$ that appears in the latter model has to be chosen equal to $1/\tau_J$ obtained from (31) [23]. It should be stressed that this effective collision frequency is not the same as the real collision frequency. A nice feature of the hard line system is that the real collision frequency can also be computed exactly, at any density (see Appendix A). The knowledge of this exact collision frequency proved of great help in testing the MD programme (see § 4). In Appendix A it is shown that, for a system consisting of hard needles with uniform mass distribution, the collision frequency (i.e. the average number of collisions that a given particle experiences per unit time) is given by

$$\Gamma \equiv \left\langle \frac{dn}{dt} \right\rangle = 1{\cdot}237662399 \ldots \rho^*. \tag{A 15}$$

The Enskog expression for the velocity autocorrelation function (ACF) is derived in Appendix B. The result is

$$\langle \mathbf{v}(0) \cdot \mathbf{v}(t) \rangle = \langle v(0)^2 \rangle \exp(-t/\tau_v), \tag{33}$$

with

$$1/\tau_v = 0{\cdot}43416 \ldots \rho^*. \tag{B 18}$$

The self diffusion coefficient D is given by :

$$D = (1/3) \int_0^\infty \langle \mathbf{v}(0) \cdot \mathbf{v}(t) \rangle \, dt = 2{\cdot}303293 \ldots /\rho^*. \tag{B 20}$$

It is convenient to make a distinction between the components of $\mathbf{v}$ that are parallel and perpendicular to the orientation of the molecule at $t = 0$. We define a longitudinal and a transverse velocity ACF by :

$$C_\parallel(t) = \langle \mathbf{v}(0) \cdot \mathbf{u}(0)\mathbf{v}(t) \cdot \mathbf{u}(0) \rangle \tag{34}$$

and

$$C_\perp(t) = \langle \mathbf{v}(0) \cdot \mathbf{P} \cdot \mathbf{v}(t) \rangle, \tag{35}$$

where $\mathbf{P} = (\mathbf{I} - \mathbf{u}(0)\mathbf{u}(0))$. For smooth hard needles, the initial slope of $C_\parallel(t)$ is zero, while the initial slope of $C_\perp(t)$ is $\frac{3}{2}$ times the Enskog value.

The Enskog expression for the angular momentum ACF is given by

$$\langle \mathbf{J}(0) \cdot \mathbf{J}(t) \rangle = \langle J(0)^2 \rangle \exp(-t/\tau_J), \tag{36}$$

with

$$1/\tau_J = 0{\cdot}58642 \ldots \rho^*. \tag{B 27}$$

In the same approximation, the correlation time of rotational energy fluctuations is given by :

$$1/\tau_\epsilon = 0{\cdot}7486168 \ldots \rho^*. \tag{B 32}$$

As was mentioned above, the use of Gordon's J-diffusion model for $C_l(t) = \langle P_l(\mathbf{u}(0) \cdot \mathbf{u}(t)) \rangle$ is consistent with the Enskog approximation for $\langle \mathbf{J}(0) \cdot \mathbf{J}(t) \rangle$ if the ' collision frequency ' in the J-diffusion model is identified with $1/\tau_J$ given by (B 27). It should be stressed, however, that even when the approximations leading to (36) are justified, the predictions of the J-diffusion model should be treated with caution. For example in the J-diffusion model it is assumed that every collision completely thermalizes the angular momentum of a colliding molecule. If this assumption were correct, the relaxation times τ_J and τ_ϵ should be equal. Actually, as (B 27) and (B 32) show, τ_ϵ is some 20 per cent shorter than τ_J, even within the Enskog approximation. Although the J-diffusion model can be generalized to include cases where τ_ϵ and τ_J are different [26], we will restrict ourselves to the model in its simplest form. Finally, we note that in the limit of high collision frequencies, the J-diffusion model predicts simple rotational diffusion behaviour :

$$C_l(t) \simeq \exp(-t/\tau_l). \tag{37}$$

In this limit, the model predicts that τ_l and τ_J should obey the Hubbard relation [27] :

$$\lim_{\rho \to \infty} (\tau_J \cdot \tau_l)^{-1} = l(l+1)kT/I. \tag{38}$$

This result is, however, independent of the details of the model and, as we will see below, a very different approach (viz. the use of scaling arguments), while leading to quite different predictions for the density dependence of τ_J and τ_l, still predicts that the product of τ_J and τ_l should tend to a constant independent of density.

3.3. *Scaling regime*

The assumption that successive binary collisions are uncorrelated, which constitutes the basis for the Enskog approach, will fail at high densities. The reason is that the translational and rotational diffusion of a molecule will be dominated by the geometrical constraints imposed by the presence of other molecules. At high densities, these constraints survive over lengths of time corresponding to many binary collisions. In situations where such geometrical constraints are important, one can arrive at qualitative predictions concerning the density dependence of a number of transport properties, using scaling arguments similar to those first presented in this context by Doi and Edwards [10, 11] (for a general reference on this subject, see [28]). The Doi–Edwards (DE) theory was developed to describe the brownian dynamics of thin rod-like macromolecules in concentrated solution. In order to apply the DE theory to the hard line fluid under consideration, two minor modifications have to be introduced: (1) between interactions the needles move freely, rather than diffusively, and (2) a collision can only change the component of the molecular velocity perpendicular to the molecular axis. This latter property which, as we will see below, has far reaching consequences, is a peculiarity of *smooth* hard needles.

Let us first consider rotational diffusion. The rotational diffusion coefficient D_r is related to the mean square angular displacement of a needle by

$$\lim_{t\to\infty} \frac{d}{dt} \langle \theta^2(t) \rangle = 4D_r. \tag{39}$$

Due to the presence of other molecules, a typical molecule cannot change its orientation appreciably unless one of the constraining molecules moves out of the way. Whenever this happens, the orientation of the molecule under consideration can ' jump ' over an angle $\delta\theta$ which is of the order ρ^{*-1} [10]. The total mean square angular displacement in a time t is then given by

$$\langle \theta^2(t) \rangle \simeq N \langle \delta\theta^2 \rangle, \tag{40}$$

where N is the number of times such an angular jump can take place in an interval t. In the case considered by DE, N/t (the rate at which the constraining molecules move out of the way) is of order $L^2/D_{\parallel}^0$, where $D_{\parallel}^0$ is the parallel component of the diffusion tensor of rods of length L, in the limit of infinite dilution. The DE expression is correct if the persistence time of the molecular velocity along the rod axis is much shorter than $L^2/D_{\parallel}^0$. In the system of smooth hard needles that we consider here, this condition is not necessarily satisfied. In fact, as we will see below, at sufficiently high densities the opposite is true (i.e. $\mathbf{v}_{\parallel}$ does *not* decay appreciably in the time it takes a molecule to cover a distance L along its axis). In the latter limit N/t is of order $L/(v_{\parallel}^2)^{1/2}$ which, in reduced units, is of order 1. The expression for the rotational diffusion constant D_r then becomes

$$D_r \sim 1/\rho^{*2}, \tag{41 a}$$

which differs from the corresponding DE expression

$$D_r \sim D_{\parallel}^{0}/\rho^{*2} \tag{41 b}$$

in that the former relation is independent of the translational diffusion constant.

Using essentially identical reasoning one arrives at the prediction that, at sufficiently high density, $D_\perp$ (the component of the molecular self-diffusion tensor, perpendicular to the molecular axis) should also go as ρ^{*-2}:

$$D_\perp \sim \rho^{*-2}. \tag{42}$$

As we know that the initial slope of $C_\perp(t) = \langle \mathbf{v}_\perp(0) \cdot \mathbf{v}_\perp(t)\rangle / \langle v_\perp(0)^2\rangle$ is given by $-(\frac{3}{2})$. $0{\cdot}43416 \cdot \rho^*$ (B 18), it is clear that, at high densities $C_\perp(t)$ must develop a negative portion with an area that almost cancels the positive area (which is proportional to ρ^{*-1}) in such a way that the remainder is proportional to ρ^{*-2}. For exactly the same reason, a negative part in the angular momentum correlation function should be expected when the rotational diffusion constant exhibits the scaling behaviour predicted by (41 *a*). In other words, even though $C_J(t)$ is not expected to be exponential at high densities, a relation of the form of (38) should still hold.

The scaling predictions for the longitudinal velocity ACF, $C_\parallel(t)$, differ quite dramatically from those for $C_\perp(t)$. This is a consequence of the fact that the impulsive force which acts on a smooth hard needle during a collision is always directed perpendicular to the rod axis. Consequently, the component of the molecular velocity that is directed along the molecular axis at $t=0$, cannot change until the molecule has rotated over some angle θ. The rate of change of $C_\parallel(t)$ can be approximated by:

$$\dot{C}_\parallel(t) = -\tfrac{3}{2}\gamma \langle \sin^2 \theta(t)\rangle C_\parallel(t), \tag{43}$$

where γ is the initial rate of change of $\langle \mathbf{v}(0) \cdot \mathbf{v}(t)\rangle$ ($\gamma = 0{\cdot}43416\rho^*$; (B 18)). For very short times ($t \ll \tau_{BC}$, with τ_{BC} = average time between collisions), we can use the free rotor expression for $\langle \sin^2 \theta(t)\rangle$:

$$\langle \sin^2 \theta(t)\rangle \simeq \langle \theta^2(t)\rangle \simeq \langle \omega^2\rangle t^2, \tag{44 a}$$

and the expression for $C_\parallel(t)$ becomes:

$$C_\parallel(t) \simeq \exp(-\gamma \langle \omega^2\rangle t^3/3). \tag{44 b}$$

For times long compared with τ_{BC}, $\theta^2(t)$ is determined by the rotational diffusion constant D_r. In particular, the probability of finding an angular displacement $\Delta\theta$ in an interval t is given by:

$$P(\Delta\theta;\ t) = (1/4\pi D_r t) \exp(-(\Delta\theta_x^2 + \Delta\theta_y^2)/4D_r t), \tag{45}$$

where $\Delta\theta_x$ and $\Delta\theta_y$ are the angular displacements along the x and y axes respectively (assuming that the molecule points along z at $t=0$). Equation (45) is valid for $\Delta\theta^2 \ll 1$. The longitudinal velocity ACF obeys the relation:

$$\frac{d}{dt} \ln(\tilde{C}_\parallel(t)) = (\tfrac{3}{2})\gamma\theta^2(t), \tag{46}$$

where we have used a tilde on $\tilde{C}_{\parallel}(t)$ to indicate that this expression still has to be averaged over all angles $\theta(t)$. From (46) it follows that :

$$C_{\parallel}(t) = \langle v^2(0)\rangle \left\langle \exp\left(- \int_0^t (\tfrac{3}{2})\gamma\theta^2(t')\, dt' \right) \right\rangle_{\theta(t')}. \tag{47}$$

The subscript $\theta(t')$ on the right hand side of (47) stands for averaging over all intermediate angles. Using (45), this can be rewritten as :

$$\begin{aligned} C_{\parallel}(t) &= \langle v_{\parallel}{}^2(0)\rangle \lim_{n\to\infty} \int_{-\infty}^{\infty} \dots \int_{-\infty}^{\infty} d\theta_1{}^x \dots d\theta_n{}^x\, d\theta_1{}^y \dots d\theta_n{}^y \left(\frac{n}{4\pi D_R t}\right)^n \\ &\qquad \times \exp\left(- \sum_{i=1}^{n} \left[\frac{(\theta_i - \theta_{i-1})^2}{4D_R t/n} + \tfrac{3}{2}\gamma\theta_i{}^2 \frac{t}{n} \right] \right) \\ &= \langle v_{\parallel}{}^2(0)\rangle \int_{-\infty}^{\infty} d\theta^x(t) \int_{-\infty}^{\infty} d\theta^y(t) \iint \mathscr{D}\theta^x(t')\mathscr{D}\theta^y(t') \\ &\qquad \times \exp\left(- \int_0^t \left(\frac{\dot{\theta}^2(t')}{4D_R} + \tfrac{3}{2}\gamma\theta^2(t') \right) dt' \right) \end{aligned} \tag{48}$$

where we have used the conventional path-integral notation [29].

The path integral appearing in (48) is elementary (it is identical to the expression for the density matrix of a two dimensional harmonic oscillator [29]). Making the appropriate substitutions, we obtain :

$$\begin{aligned} C_{\parallel}(t) &= \langle v_{\parallel}{}^2(0)\rangle \left(\int_{-\infty}^{\infty} d\theta^x(t) \left(\frac{(3\gamma/2D_R)^{1/2}}{\pi \sinh\left(t\sqrt{(6\gamma D_R)}\right)} \right)^{1/2} \right. \\ &\qquad \left. \times \exp\left[-(3\gamma/2D_R)^{1/2} \coth\left(t\sqrt{(6\gamma D_R)}\right)\theta^{x2}(t) \right] \right)^2 \\ &= \left(\cosh\left(t\sqrt{(6\gamma D_R)}\right)\right)^{-1} \langle v_{\parallel}{}^2(0)\rangle. \end{aligned} \tag{49}$$

Using (49), it immediately follows that the longitudinal diffusion coefficient $D_{\parallel}$ is given by :

$$D_{\parallel} = \int_0^{\infty} C_{\parallel}(t)\, dt = \pi/(6\gamma D_r)^{1/2}. \tag{50}$$

As $\gamma \sim \rho^*$ and $D_r \sim \rho^{*-2}$, it follows that :

$$D_{\parallel} \sim \rho^{*1/2}.$$

We are thus led to the remarkable conclusion that $D_{\parallel}$ should diverge as $\rho^* \to \infty$! In fact, we arrived at essentially the same conclusion in (12), but the line of reasoning followed in that publication is based on simplifications in the integration of (46) that are not warranted as $t \to \infty$. It could be argued that the assumption $\theta^2 \ll 1$ limits the validity of (49) to times $t \ll D_r{}^{-1}$. However, the physical content of (49) is that for longer times only those molecules which have *not* rotated over large angles continue to contribute to $C_{\parallel}(t)$. Although the replacement of sin θ by θ in (46) will most likely lead us to overestimate the rate of decay of $C_{\parallel}(t)$ (and hence underestimate $D_{\parallel}$), we expect (49) to be, at least qualitatively, correct.

To end this section on scaling predictions for transport properties of the hard needle fluid, we want to give a rough estimate of the density above which scaling effects should become important. In order to arrive at such an estimate, we note that the essential feature of the scaling approach is that it assumes

geometrical constraints on the position and orientation of molecules. Suppose we select any given molecule and choose our z-axis along the molecular axis, such that $z=0$ coincides with the centre of mass of the molecule. Next we project all molecules i, with $-L/2 \leqslant z_i \leqslant L/2$, onto the plane $z=0$. It is clear that the transverse motion of the molecule under consideration is geometrically constrained to a *finite* region if the projections of the other molecules form a network with *finite* void spaces in between. In other words, the onset of scaling behaviour is related to a two dimensional percolation transition. We can arrive at a lower estimate of this percolation transition by noting that the average number of molecules (or rather, projections of molecules) intersecting the projection of any given molecule must be larger than 2 [30]. This implies that the reduced 2-D density $\rho_{2D}^* = \rho_{3D}^*(\langle L_{2D}^2 \rangle / L^2)$ must satisfy the following inequality :

$$\rho_{2D}^*(2/\pi) > 2, \tag{51}$$

and hence

$$\rho_{3D}^* > (3\pi/2) \simeq 4{\cdot}5, \tag{52}$$

where we have used the fact that $\langle L_{2D}^2 \rangle = (\frac{2}{3})L^2$. We stress that (52) provides a *lower limit* to scaling behaviour. In fact, we should expect clear manifestations of scaling behaviour only at densities well above $\rho^* = (3\pi/2)$.

4. Results

4.1. *Computational aspects*

Molecular dynamics simulations were performed on a system consisting of N hard needles ($N=100$ and $N=500$) at densities ranging from $\rho^*=1$ to $\rho^*=48$. On a CYBER 170–750 computer a typical run (20 000 collisions) took about 1500 CPU seconds for a 100 particle system and between 2800 and 4500 s for a 500 particle system (the longer runs correspond to higher densities). Although

Table 1. Summary of relevant parameters characterizing the different MD runs referred to in the text. Reduced densities (ρ^*) have been tabulated in column 1, the systems sizes (N) are given in column 2. In column 3, N_c stands for the number of collisions per simulation. Columns 4 and 5 show a comparison of the measured (Γ_{MD}) and predicted (Γ_{TH}) collision frequencies.

ρ^*	N	N_c	MD	TH
1	100	20000	1.24	1·24
2	100	20000	2·44	2·48
4	100	20000	4·89	4·95
5	100	20000	6·14	6·19
6	100	20000	7·24	7·43
8	100	20000	9·99	9·90
16	500	20000	19·8	19·8
24	500	20000	30·2	29·7
32	500	20000	40·0	39·6
40	500	30000	49·8	49·5
48	500	50000	60·8	59·4

the present simulations are about an order of magnitude slower than the simulation of comparable hard sphere systems, the runs were long enough to obtain acceptable statistics on most single particle properties (the estimated error is of the order of 1–2 per cent). As has been explained in § 2, fully equilibrated initial configurations can easily be generated and hence there is no need for equilibration runs. Table 1 summarizes the conditions for the different simulations that we performed. As can be seen from this table, the collision frequencies found in the simulations agree quite well with the predictions based on (A 15).

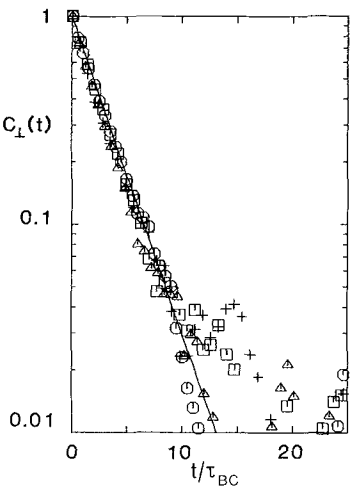

Figure 5. Transverse velocity ACF $C_\perp(t)$ (see (35)) as a function of time t (expressed in collision times). $\rho^*=1$, □; $\rho^*=2$, ○; $\rho^*=4$, △; $\rho^*=6$, +. The drawn line is the Enskog prediction, (33).

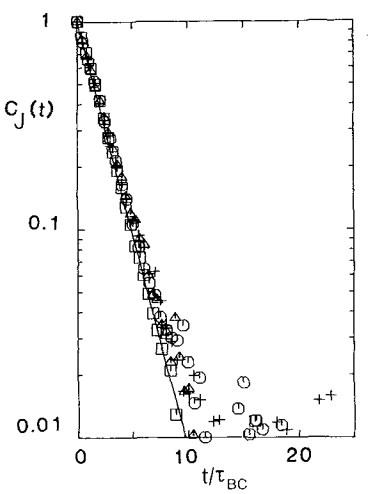

Figure 6. Angular momentum ACF $C_J(t)$ as a function of time t (expressed in collision times). $\rho^*=1$, □; $\rho^*=2$, ○; $\rho^*=4$, △; $\rho^*=6$, +. The drawn line is the Enskog prediction, (36).

At high densities, where we expect fluctuations to decay slowly, the noise in the measured collision frequency appears to increase somewhat. For example, the value 60·8 at $\rho^* = 48$ is the average of two subruns with collision frequencies differing by well over 1 per cent. The results shown in table 1 give no reason to believe that collisions are overlooked by the algorithm described in § 2 (if this were the case, the measured collision frequencies would be systematically lower than the value given by (A 15)).

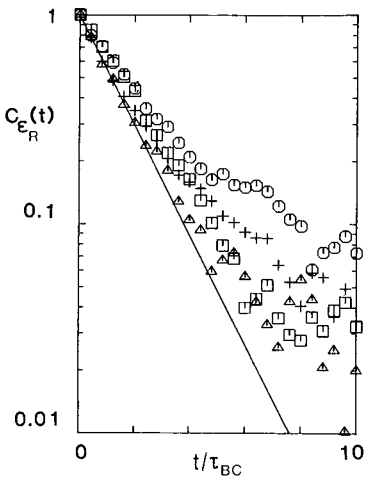

Figure 7. Rotational energy ACF $C_{\epsilon_R}(t)$ as a function time t (expressed in collision times). $\rho^* = 1$, □; $\rho^* = 2$, ○; $\rho^* = 4$, △; $\rho^* = 6$, +. The drawn line is the Enskog prediction (see Appendix B.3).

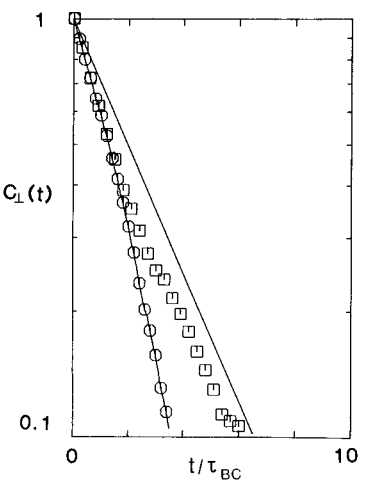

Figure 8. Transverse velocity ACF at $\rho^* = 8$ (□) and $\rho^* = 48$ (○). The time scale has been expanded to show the short time behaviour more clearly. Both curves are well below the Enskog prediction (drawn straight line). The initial slope of $C_\perp(t)$ is $\frac{3}{2}$ times larger than the Enskog prediction.

4.2. *Low density behaviour*

Let us next consider the Enskog predictions for the translational and rotational correlation functions. We found that in every case studied, the initial slopes of the correlation functions of **v**, **J** and $\Delta\epsilon_r$ did indeed follow the Enskog predictions. The correlation functions of $\mathbf{v}_\perp(t)$, $\mathbf{J}(t)$ and $\Delta\epsilon_r(t)$ at low densities ($\rho^* < 8$) are compared with the appropriate Enskog predictions in figures 5, 6 and 7. Out to

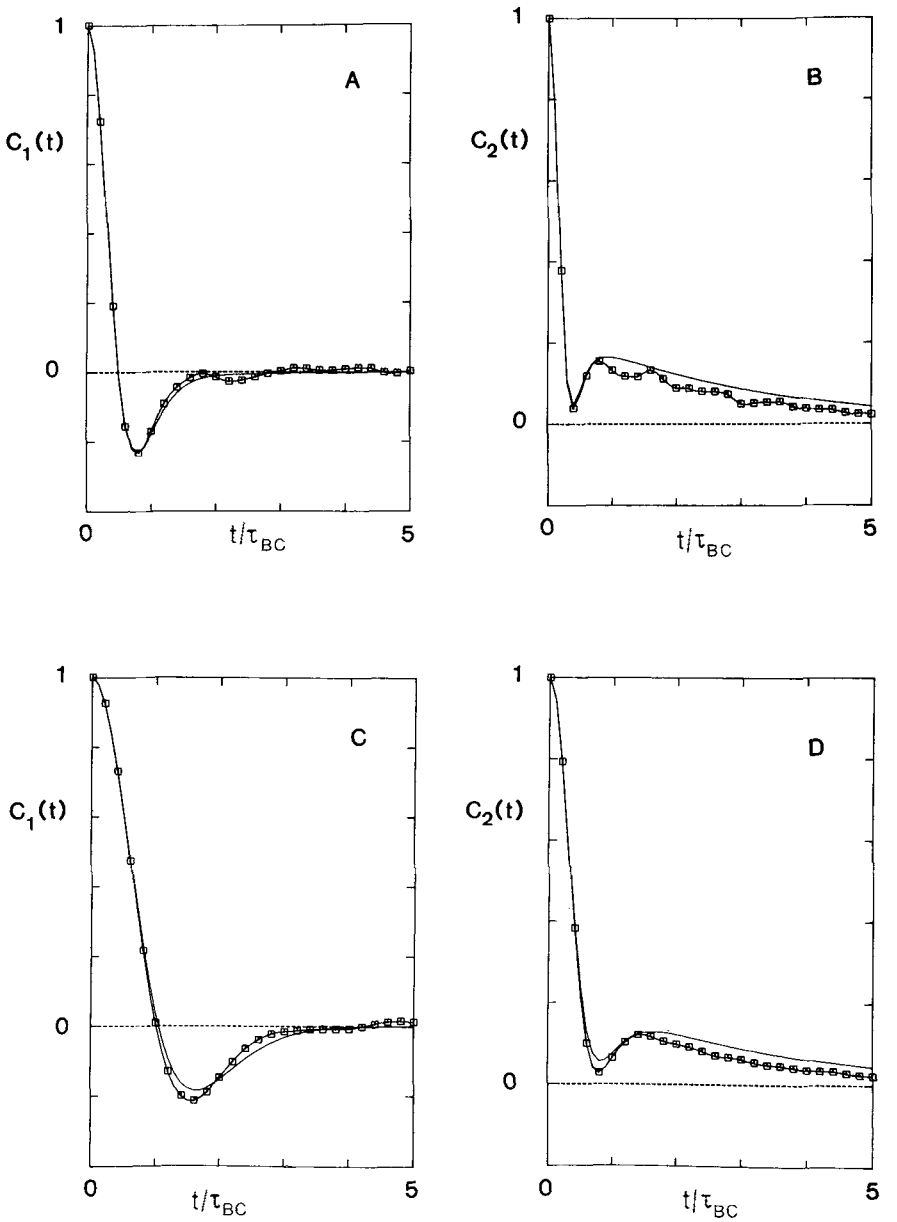

Figure 9. Comparison of MD data for the orientational correlation functions $C_1(t)$ and $C_2(t)$ (see text) with the corresponding J-diffusion predictions. MD-data, □; J-diffusion, drawn curve. $(A+B)$, $\rho^*=1$; $(C+D)$, $\rho^*=2$. The time is in units of average time between collisions.

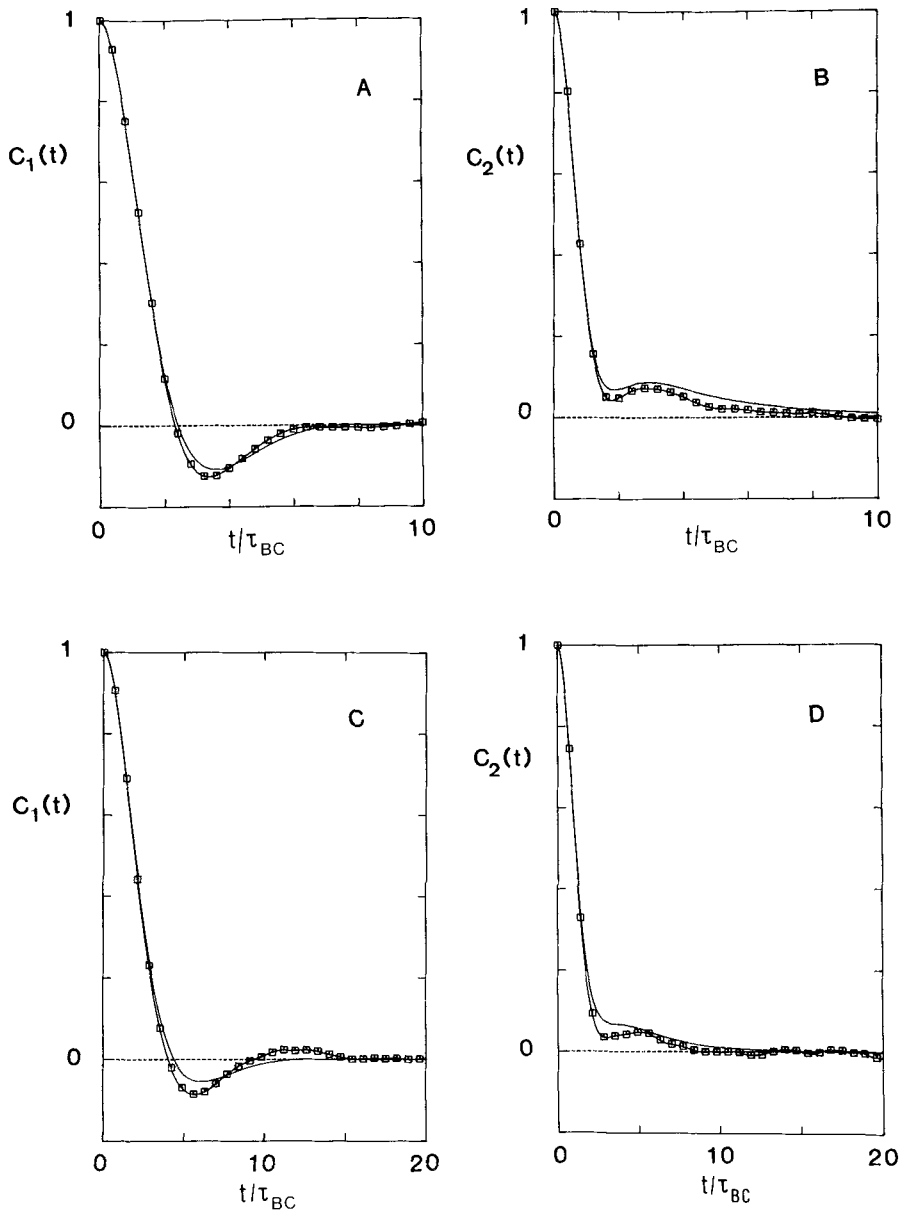

Figure 10. Comparison of MD data for the orientational correlation functions $C_1(t)$ and $C_2(t)$ (see text) with the corresponding J-diffusion predictions. $(A+B)$, $\rho^*=4$; $(C+D)$, $\rho^*=6$. The meaning of all other symbols is the same as in figure 9.

about 10 collision times, $\langle \mathbf{v}_\perp(0) \cdot \mathbf{v}_\perp(t) \rangle$ (figure 5) follows the Enskog predictions almost quantitatively. Actually, the initial slope of $\langle \mathbf{v}_\perp(0) \cdot \mathbf{v}_\perp(t) \rangle$ is found to be $\frac{3}{2}$ times the Enskog value (as it should), but after a few collision times the correlation function changes over to an exponential with decay time τ_v given by (B 18) (see figure 8). $\langle \mathbf{J}(0) \cdot \mathbf{J}(t) \rangle$ (figure 6) is seen to follow the Enskog predictions very well, considering that the estimated noise level in the correlation

function is 1–2 per cent. The agreement of $\langle \Delta\epsilon_r(0)\Delta\epsilon_r(t)\rangle$ with the Enskog predictions is somewhat less impressive (figure 7). These correlation functions seem to deviate from simple exponential decay well before they are swamped by the (rather high) noise. The existence of two timescales in the decay of rotational energy fluctuations would not be surprising : one should expect one timescale characteristic of the decay of rotational energy fluctuations to a value corresponding to the local temperature, while fluctuations in the local temperature should decay on a somewhat longer timescale. The quality of the MD data did not warrant a comparison with a more detailed theory. Using a ' collision frequency ' $1/\tau_J$ (B 27), we have computed the J-diffusion predictions for $\langle P_1(\mathbf{u}(0)\,.\,\mathbf{u}(t))\rangle$ and $\langle P_2(\mathbf{u}(0)\,.\,\mathbf{u}(t))\rangle$. For densities $\rho^* < 8$, these predictions tend to agree very well with the measured correlation functions (figures 9 and 10). In table 2 the measured correlation times τ_1 and τ_2 are compared with the J-diffusion predictions. In the same table we also present the area under the normalized angular momentum ACF, and the longitudinal, transverse and average diffusion constants. The average (trace) diffusion constant D is defined as $D=(D_\parallel+2D_\perp)/3$. The average diffusion constant follows the Enskog predictions quite well for $\rho^* < 8$. Figure 11 shows the low-density behaviour of the longitudinal velocity correlation function, $C_\parallel(t)$. The initial slope of $C_\parallel(t)$ is zero (see (44)) but this is barely visible for $\rho^* < 6$. For $\rho^* = 1$, 2 and 4 $C_\parallel(t)$ fits fairly well to the Enskog predictions ; the behaviour of $C_\parallel(t)$ at $\rho^* = 6$ (positive deviation from Enskog) is a precursor of the much larger positive deviations that appear at higher densities.

Table 2. Summary of measured and predicted values for the orientational correlation times τ_1 and τ_2, the angular momentum correlation time τ_J and the translational diffusion constant $D=(D_\parallel+2D_\perp)/3$. The superscripts E stand for the Enskog (c.q. J-diffusion) predictions described in the text. The superscript S stands for the scaling approximation (50). The entries without superscript refer to the MD data.

ρ^*	τ_1	τ_1^E	τ_2	τ_2^E	τ_J	τ_J^E	D	D^E	$D_\perp$	$D_\parallel$	$D_\parallel^S$
1	0·12	0·10	0·49	0·61	1·69	1·71	2·40	2·30	2·30	2·59	—
2	0·14	0·14	0·30	0·35	0·93	0·85	1·16	1·15	1·05	1·37	—
4	0·21	0·20	0·22	0·24	0·44	0·43	0·61	0·58	0·51	0·82	—
6	0·25	0·25	0·17	0·21	0·31	0·28	0·44	0·38	0·36	0·60	—
8	0·30	0·29	0·18	0·21	0·20	0·21	0·34	0·29	0·25	0·53	—
16	0·51	0·47	0·23	0·23	0·088	0·11	0·24	0·14	0·11	0·50	0·42
24	0·73	0·65	0·36	0·28	0·058	0·071	0·21	0·096	0·073	0·49	0·43
32	0.93	0·83	0·36	0·33	0·039	0·053	0·20	0·072	0·049	0·50	0·44
40	1·27	1·02	0·43	0·38	0·029	0·043	0·23	0·058	0·031	0·64	0·53
48	2·01	1·21	0·68	0·44	0·025	0·036	0·34	0·048	0·025	0·97	0·56

4.3. *High density behaviour*

The behaviour of the same correlation functions at $\rho^* > 8$ tends to exhibit pronounced deviations from the Enskog predictions. The only exception is $\langle \Delta\epsilon_r(0)\Delta\epsilon_r(t)\rangle$ (figure 12) which behaves in much the same way as at low densities. One may argue that this is not really surprising because the geometrical constraints which become important at high densities are not expected

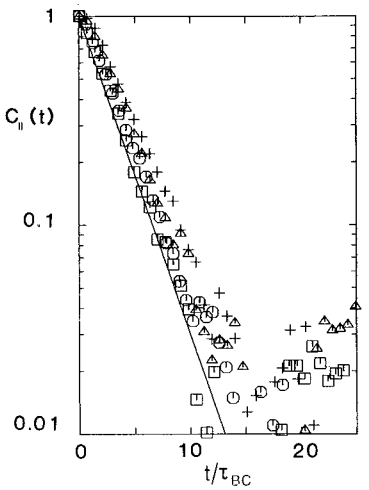

Figure 11. Longitudinal velocity ACF $C_{\parallel}(t)$ (see (34)) as a function of time t (expressed in collision times). $\rho^*=1$, □; $\rho^*=2$, ○; $\rho^*=4$, △; $\rho^*=6$, +. The drawn line is the Enskog prediction, (33).

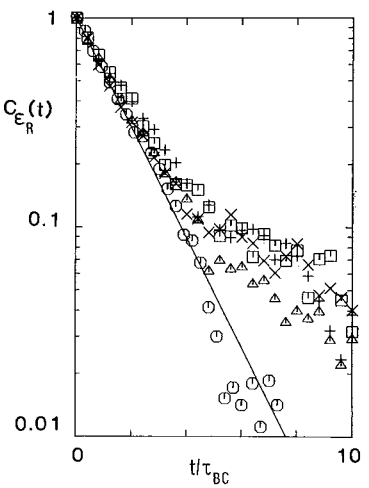

Figure 12. Rotational energy ACF $C_{\epsilon_R}(t)$ as a function of time (expressed in collision times). $\rho^*=8$, □; $\rho^*=16$, ○; $\rho^*=24$, △; $\rho^*=32$, +; $\rho^*=48$, ×. The drawn line is the Enskog prediction (see Appendix B.3).

to have any strong effect on rotational energy relaxation. In contrast, the transverse velocity correlation function, $C_{\perp}(t)$, becomes strongly non-exponential at high densities; $C_{\perp}(t)$ falls consistently below $\exp(-t/\tau_v)$. At the highest densities studied, $C_{\perp}(t)$ even goes negative after a few collision times (figure 13). This behaviour, which is reminiscent of the behaviour of $\langle \mathbf{v}(0) \cdot \mathbf{v}(t) \rangle$ in a hard sphere fluid [1], is compatible with the scaling predictions of § 3. In fact, $(D_{\perp}-D_E)/D_{\perp}$ (D_E stands for D_{Enskog}) fits quite well to a straight line through the origin of the form $(D_{\perp}-D_E)/D_{\perp} = -0{\cdot}017\rho^*$, which supports the scaling

prediction $D_\perp \sim \rho^{*-2}$. The high density behaviour of $\langle \mathbf{J}(0) \cdot \mathbf{J}(t) \rangle$ strongly resembles that of $C_\perp(t)$; $\langle \mathbf{J}(0) \cdot \mathbf{J}(t) \rangle$ becomes non-exponential and gradually develops a negative part (figure 14). Such behaviour is to be expected if the scaling approach described in § 3 is appropriate. A fit of $(\tau_J{}^E - \tau_J)/\tau_J$ (where $\tau_J{}^E$ stands for the Enskog value given by (B 27)) to a straight line through the origin yields a fair fit with a slope of 0·009 (in this fit we only included the high density points ($\rho^* > 8$)). With increasing density the orientational correlation functions $C_1(t) = \langle P_1(\mathbf{u}(0) \cdot \mathbf{u}(t)) \rangle$ and $C_2(t) = \langle P_2(\mathbf{u}(0) \cdot \mathbf{u}(t)) \rangle$ fit progressively worse to the corresponding J-diffusion expressions. At high densities it is found that the actual decay of $C_1(t)$ and $C_2(t)$ is slower than the J-diffusion model

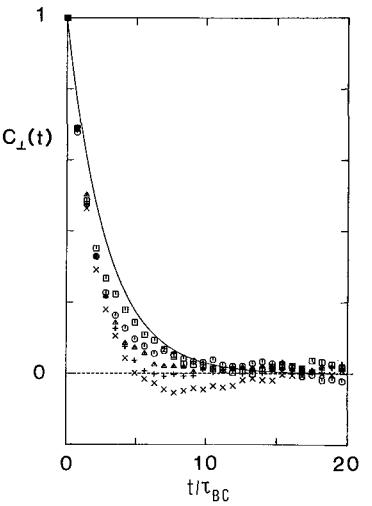

Figure 13. Transverse velocity ACF $C_\perp(t)$ (see (35)) as a function of time t (expressed in collision times). $\rho^* = 8$, □; $\rho^* = 16$, ○; $\rho^* = 24$, △; $\rho^* = 32$, +; $\rho^* = 48$, ×. The drawn curve is the Enskog prediction (33).

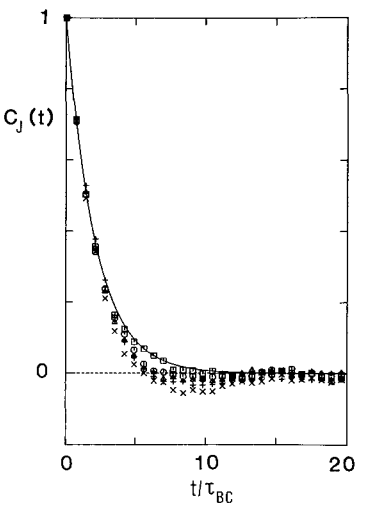

Figure 14. Angular momentum ACF $C_J(t)$ as a function of time t (expressed in collision times). $\rho^* = 8$, □; $\rho^* = 16$, ○; $\rho^* = 24$, △; $\rho^* = 32$, +; $\rho^* = 48$, ×. The drawn curve is the Enskog prediction, (36).

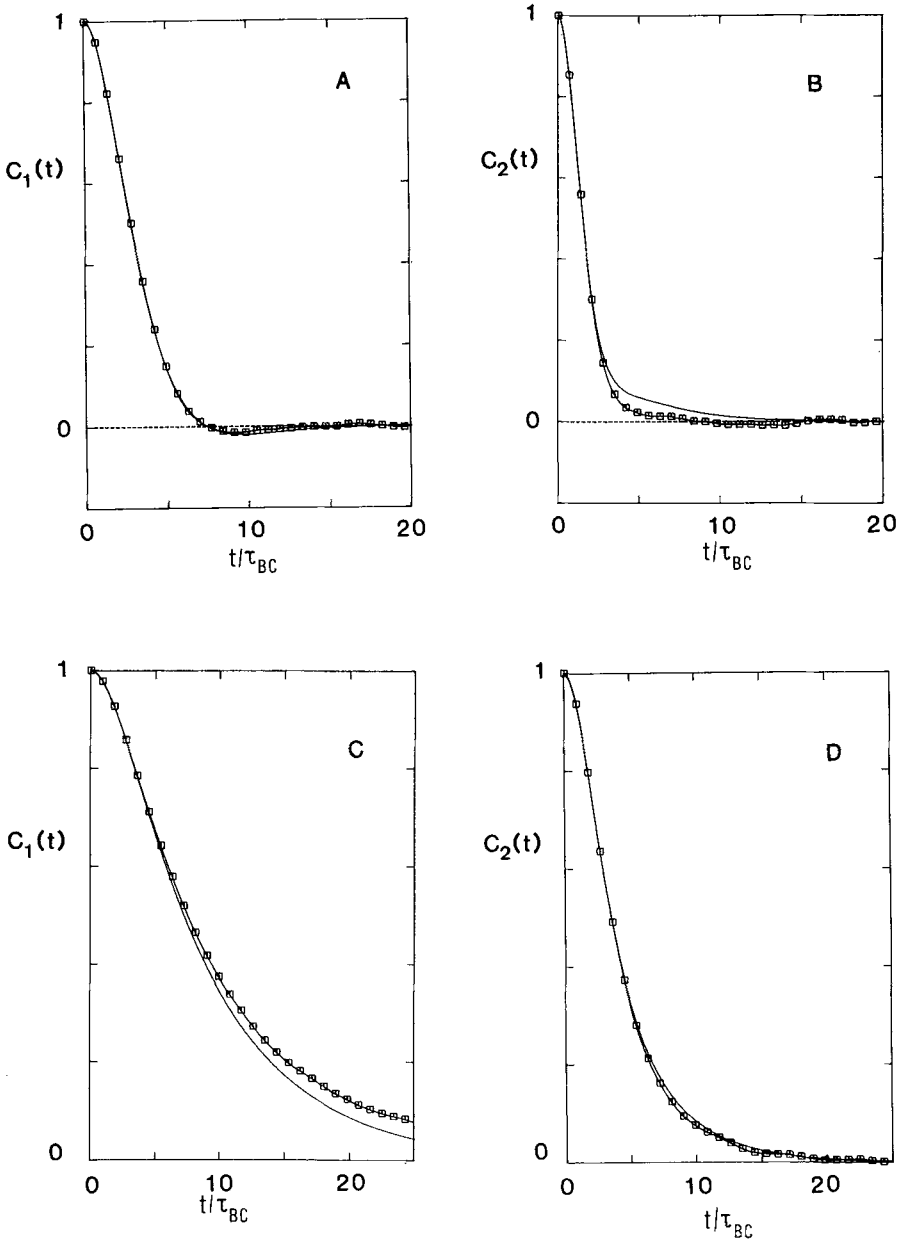

Figure 15. Comparison of MD data for the orientational correlation functions $C_1(t)$ and $C_2(t)$ (see text) with the corresponding J-diffusion predictions. $(A+B)$, $\rho^*=8$; $(C+D)$, $\rho^*=16$. The meaning of all other symbols is the same as in figure 9.

would predict (figure 15–17). This is related to the fact that, at high densities, τ_J becomes significantly smaller than the Enskog value $\tau_J{}^E$. The opposite effect has been observed by O'Dell and Berne [19] in their study of the rough-sphere fluid. In the latter system τ_J becomes larger than $\tau_J{}^E$ at high densities, and as a consequence $C_1(t)$ and $C_2(t)$ decay *faster* than the J-diffusion model would

predict. In the present case we can achieve better agreement between J-diffusion and the MD data by equating the J-diffusion ' collision frequency ' to $1/\tau_J$, where τ_J is the *real* correlation time of the angular momentum ACF, rather than the Enskog expression. A more quantitative measure of the slowing down of reorientational motion at high densities is given by the correlation times

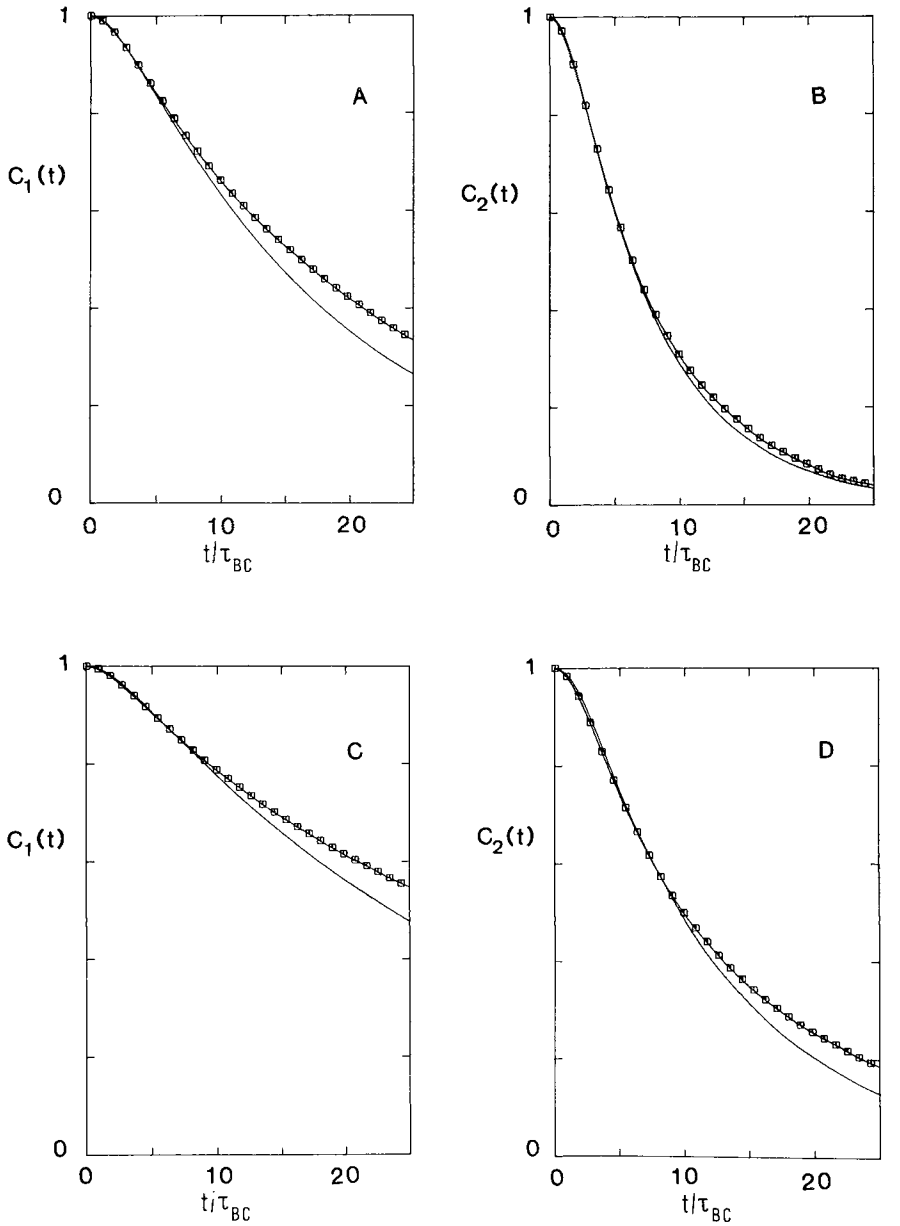

Figure 16. Comparison of MD data for the orientational correlation functions $C_1(t)$ and $C_2(t)$ (see text) with the corresponding J-diffusion predictions. $(A+B)$, $\rho^*=24$; $(C+D)$, $\rho^*=32$. The meaning of all other symbols is the same as in figure 9.

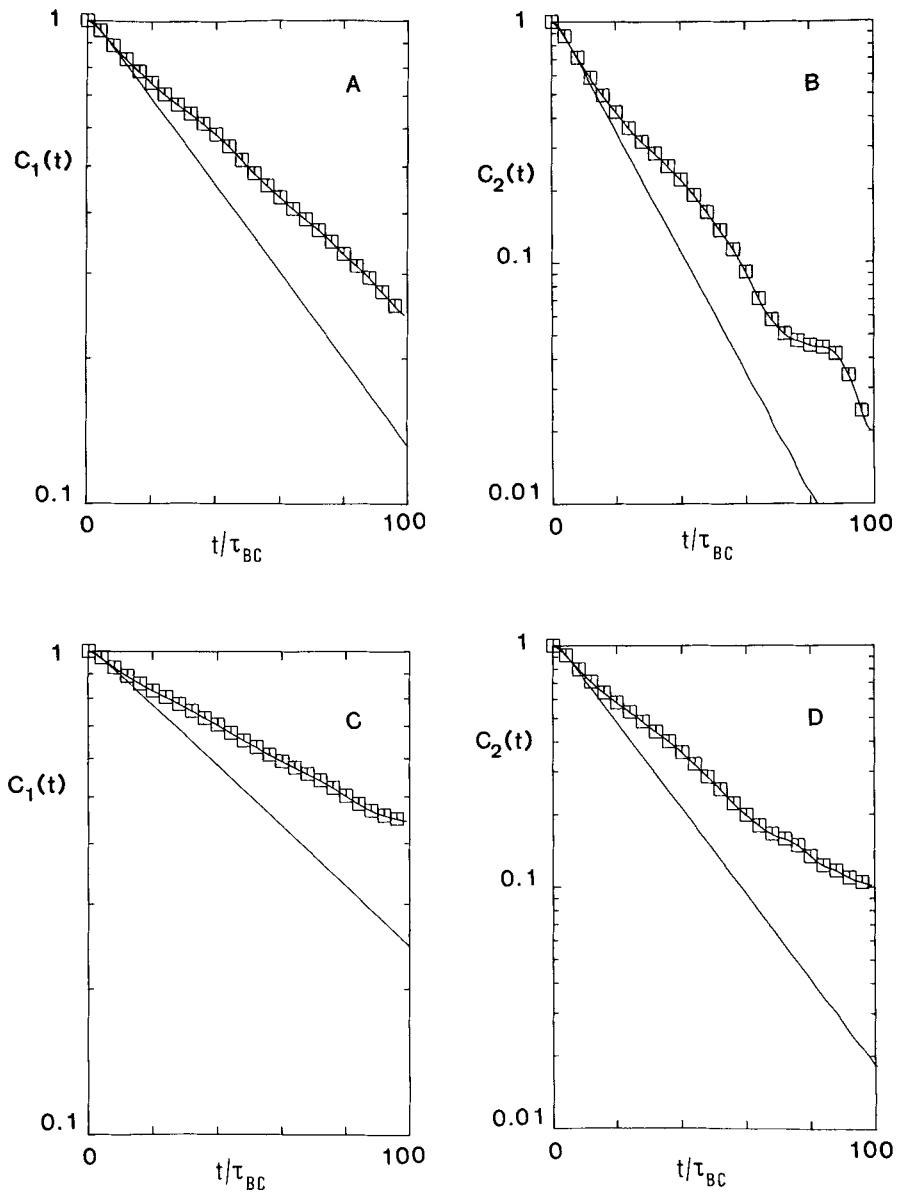

Figure 17. Comparison of MD data for the orientational correlation functions $C_1(t)$ and $C_2(t)$ (see text) with the corresponding J-diffusion predictions. $(A+B)$, $\rho^*=40$; $(C+D)$, $\rho^*=48$. The meaning of all other symbols is the same as in figure 9.

τ_1 and τ_2 shown in table 2. In § 3 we argued that in the scaling regime $D_r \sim \rho^{*-2}$. We have extracted D_r from the measured correlation functions $C_1(t)$ and $C_2(t)$ using the relation

$$C_l(t) \simeq \exp(-l(l+1)D_r t). \tag{53}$$

This relation will not be appropriate at low densities; in fact, the approximate validity of (53) *defines* the rotational diffusion regime. If $C_1(t)$ and $C_2(t)$ were

purely exponential we could have equated D_r to $(l(l+1)\tau_l)^{-1}$, with τ_l from table 2. However, as $C_1(t)$ and $C_2(t)$ only become exponential after a number of collision times it is preferable to extract D_r from the limiting slopes of $ln\,(C_l(t))$. In figures 18 and 19 we show the dependence of D_r^{-1} on ρ^{*2}. Note that the values for D_r derived from $C_1(t)$ and $C_2(t)$ agree quite well, which serves as a check that we are indeed in the rotational diffusion regime where (53) should apply. As is clear from figure 19 the dependence of D_r^{-1} on ρ^* is certainly

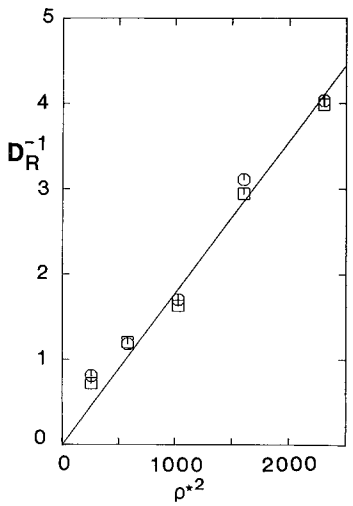

Figure 18. Dependence of the inverse rotational diffusion constant D_R^{-1} on the square of the reduced density (ρ^{*2}). D_R has been obtained from the limiting slopes of ln $C_1(t)$ (□) and ln $C_2(t)$ (○). As can be seen from the figure the points with $\rho^* \geqslant 24$ fit quite well to a straight line.

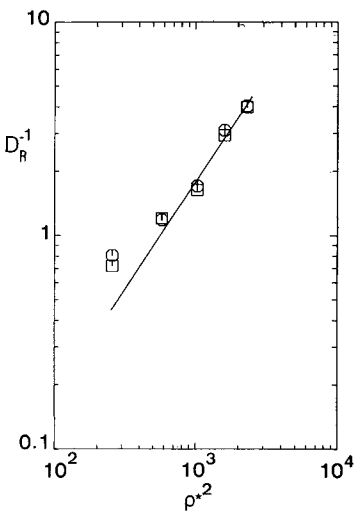

Figure 19. Log–log representation of figure 18. From the fiture it is clear that a power-law relation of the form $D_R^{-1} \sim \rho^{*2}$ is compatible with the points with $\rho^* \geqslant 24$. Meaning of symbols as in figure 18.

compatible with a quadratic relation. A fit of $-\log(D_r)$ to $(a \,.\, \log(\rho^*)+b)$ yields an exponent $a=1{\cdot}8\pm0{\cdot}2$ if we include all points with $\rho^*\geqslant 24$. If we only fit the three highest density points the exponent becomes $a=2{\cdot}2\pm0{\cdot}3$. It is worth pointing out that these results differ somewhat from those presented in [12]. The reason is that we have in the meantime obtained much better statistics on the high-density points. The conclusions drawn in [12] are however, if anything, strengthened by the present results.

Let us now consider the high density behaviour of the longitudinal velocity correlation function $C_\parallel(t)=\langle \mathbf{v}(0) \,.\, \mathbf{u}(0)\mathbf{v}(t) \,.\, \mathbf{u}(0)\rangle$. It has been argued in § 3 that in the scaling regime $C_\parallel(t)$ should show marked positive deviations from the Enskog predictions. Figure 20 shows that at densities above $\rho^*=8$ the deviations become dramatic indeed. Note that for $\rho^*\geqslant 16$ $C_\parallel(t)$ still persists after 25 collision times. At the highest densities (figure 21) $C_\parallel(t)$ even persists after 100 collision times! Because of these long decay times the statistics on $C_\parallel(t)$ become worse than at low densities as the signal-to-noise ratio is approximately determined by $(NT/\tau_D)^{1/2}$, where N is the number of particles, T is the duration of the run and τ_D is a characteristic decay time [31, 32]. At high densities τ_D becomes of the order of T and hence the signal-to-noise ratio is $\sim(N)^{1/2}$, which, for $N=500$, corresponds to an error in the correlation function of ~ 5 per cent. The same, incidentally, holds for $C_1(t)$ and $C_2(t)$ at high densities. Because of the slow decay of $C_\parallel(t)$ the longitudinal diffusion coefficient, $D_\parallel$, becomes very much larger than the Enskog value (see table 2). Moreover, at densities higher than $\rho^*\simeq 24$, $D_\parallel$ increases with increasing density! In § 3 we predicted that, in the scaling regime, $D_\parallel$ should in fact diverge as $\rho^{*1/2}$ (see (50)). Although the present data do indeed suggest that $D_\parallel$ does diverge as $\rho^*\to\infty$, this divergence appears somewhat stronger than $\rho^{*1/2}$. Using the expression for $D_\parallel$ given in (50), we obtain estimates for $D_\parallel$ that are of the right order of magnitude (see table 2), but apparently underestimate $D_\parallel$ at high densities.

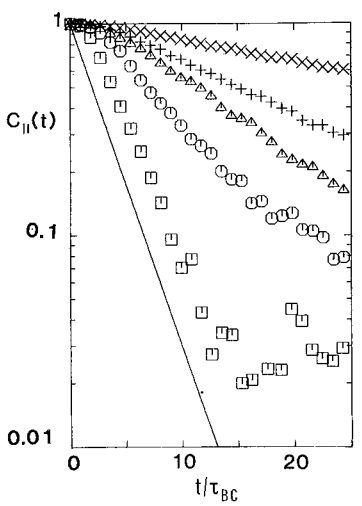

Figure 20. Longitudinal velocity ACF $C_\parallel(t)$ (see (34)) as a function of time t (expressed in collision time). $\rho^*=8$, □ ; $\rho^*=16$, ○ ; $\rho^*=24$, △ ; $\rho^*=32$, + ; $\rho^*=48$, ×. The drawn line is the Enskog prediction, (33).

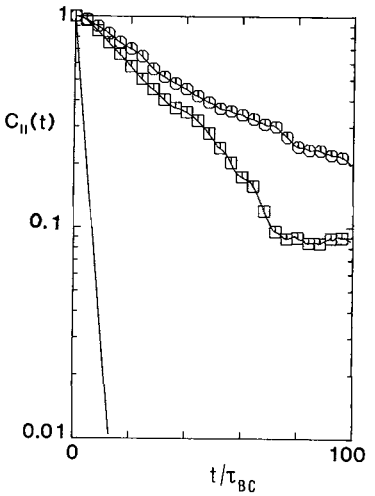

Figure 21. This figure illustrates the extremely slow decay of the longitudinal velocity ACF $C_{\parallel}(t)$ at high densities ($\rho^*=40$, □; $\rho^*=48$, ○). The drawn line is the Enskog prediction, (33).

It was mentioned in § 3 that the approximations used in the derivation of (50) would lead us to underestimate $D_{\parallel}$. Whether this indeed accounts for the effect that we are observing is not clear at present.

Finally, we wish to mention another interesting aspect of the hard needle fluid, concerning collective reorientational motions. One can define a collective orientational correlation function $C_l^c(t)$ by:

$$C_l^c(t)=N^{-1}\sum_{i=1}^{N}\sum_{j=1}^{N}(4\pi/2l+1)\sum_{m=-l}^{l}Y_{lm}^*(\mathbf{u}_i(0))Y_{lm}(\mathbf{u}_j(t)), \tag{54}$$

where Y_{lm} denotes a spherical harmonic and $\mathbf{u}_j(t)$ is the unit vector specifying the orientation of molecule j at time t. A simple two-variable theory [33, 34] yields the following relation between the collective decay time

$$\tau_l^c\left(=\int_0^\infty C_l^c(t)\,dt\right)$$

and the single particle decay time $\tau_l^s(=(l(l+1)D_r)^{-1}$:

$$\tau_l^c=((1+g_l)/(1+f_l))\tau_l^s, \tag{55}$$

where g_l is a static orientational correlation factor

$$\left(g_l=\sum_{j\neq i}\langle P_l(\mathbf{u}_j\,.\,\mathbf{u}_i)\rangle\right)$$

and f_l the corresponding dynamic correlation factor. Experimentally it has been found that single particle and collective reorientation times do indeed differ [35]. It is, however, virtually impossible to extract both g_l and f_l from such experiments. More often than not it is assumed that f_l in fact vanishes and that the difference between τ_l^c and $\tau_l t$ is due to static correlations alone. An interesting thing about the hard needle fluid is that all static correlations vanish identically

(i.e. all $g_l = 0$) and hence any difference between τ_l^c and τ_l^s is necessarily due to dynamic correlations. Unfortunately, an accurate determination of τ_l^c requires an inordinate amount of computer time as the signal to noise ratio in $C_l^c(t)$ is of order $(T/\tau_l^c)^{1/2}$. To get the statistical errors down to the 1 per cent level would require runs that are 100 (at low densities) to 10 000 (at high densities) longer than the runs that we undertook. Nevertheless, we have tried to look for systematic differences between τ_2^c and τ_2^s in the hope that, if $|f_2|$ turns out to be very large, the effect should be observable, even for relatively short simulations such as we performed. At low densities ($\rho^* = 5$) we found that $C_2^s(t)$ and $C_2^c(t)$ resemble one another closely (figure 22 A). At high densities ($\rho^* = 40$ and $\rho^* = 48$) $C_2^c(t)$ is very noisy indeed (estimated noise level ~ 40 per cent). However, in both cases we find that $C_2^c(t)$ remains consistently below $C_2^s(t)$, suggesting that $f_2 > 0$. We do not consider these results as anything even remotely resembling convincing evidence, yet we mention these preliminary data because we feel that they deserve being looked into more closely.

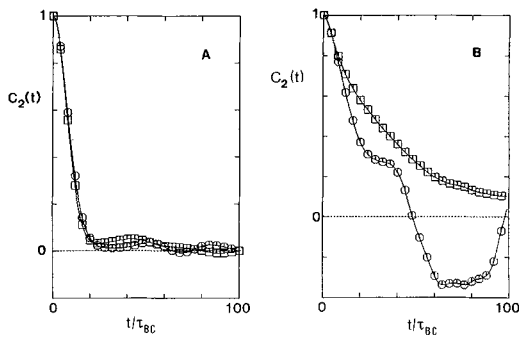

Figure 22. Comparison of the single particle (□) and collective (○) orientational correlation function $C_2(t)$ (see (54)). (A) $\rho^* = 5$; (B) $\rho^* = 48$. The noise in the collective correlation function at high densities is very large, especially for long times.

Appendix A

Consider two needles i and j which are about to collide. The position of the point of impact, $\mathbf{r}_0$, is given by

$$\mathbf{r}_0 = \mathbf{r}_i + \alpha \mathbf{u}_i = \mathbf{r}_j + \beta \mathbf{u}_j. \tag{24}$$

If we fix our frame of reference to molecule j (say) then the number of molecules i with impact distances between α and $\alpha + d\alpha$ which collide with molecule j at an impact point between β and $\beta + d\beta$ in an interval dt is given by

$$dn = \rho \sin\theta \, d\alpha \, d\beta (\Delta v_{\mathrm{imp}})_\perp 2 \, dt \, d\cos\theta/2. \tag{A 1}$$

Here ρ is the number density of molecules i, θ is the angle between $\mathbf{u}_i$ and $\mathbf{u}_j$ and $(\Delta v_{\mathrm{imp}})_\perp$ is the perpendicular component of the relative velocity of molecules i and j *at the point of impact* (see (29–30)). The factor 2 on the right hand side of (A 1) results because a collision would also take place if we were to replace the angle θ by $\theta + \pi$. From (A 1) it follows that the average collision frequency is

of the form

$$\left\langle \frac{dn}{dt} \right\rangle = \rho \int_0^{\pi} d\theta \sin^2\theta \int_{-L/2}^{L/2} d\alpha \int_{-L/2}^{L/2} d\beta \langle \Delta v_{\text{imp}})_{\perp} \rangle$$
$$= \frac{\pi}{2} \rho \int_{-L/2}^{L/2} d\alpha \int_{-L/2}^{L/2} d\beta \langle (\Delta v_{\text{imp}})_{\perp} \rangle. \tag{A 2}$$

The unaveraged relative velocity at impact is given by

$$\Delta \mathbf{v}_{\text{imp}} = \mathbf{v}_i - \mathbf{v}_j + \alpha \boldsymbol{\omega}_i \wedge \mathbf{u}_i - \beta \boldsymbol{\omega}_j \wedge \mathbf{u}_j. \tag{A 3}$$

Let us denote the unit vector perpendicular to $\mathbf{u}_i$ and $\mathbf{u}_j$ by $\mathbf{u}_{\perp}$. The component of $\Delta \mathbf{v}_{\text{imp}}$ perpendicular to $\mathbf{u}_i$ and $\mathbf{u}_j$ is

$$(\Delta v_{\text{imp}})_{\perp} = (\mathbf{v}_i - \mathbf{v}_j) \,.\, \mathbf{u}_{\perp} + \alpha \omega_i{}^{\perp} - \beta \omega_j{}^{\perp}, \tag{A 4}$$

where $\omega_i{}^{\perp}(\omega_j{}^{\perp})$ are the components of $\boldsymbol{\omega}_i(\boldsymbol{\omega}_j)$ perpendicular to $\mathbf{u}_{\perp}$. $(\Delta v_{\text{imp}})_{\perp}$ is determined by three independent variables $v_{\text{rel}\perp}(=(\mathbf{v}_i - \mathbf{v}_j) \,.\, \mathbf{u}_{\perp})$, $\omega_i{}^{\perp}$ and $\omega_j{}^{\perp}$ which are all distributed according to a one dimensional Maxwell-Boltzmann distribution :

$$P(v_{\text{rel}}{}^{\perp}, \omega_i{}^{\perp}, \omega_j{}^{\perp}) = (\mu/2\pi kT)^{1/2} (I/2\pi kT)$$
$$\times \exp\left(-(\mu v_{\text{rel}}{}^{\perp 2} + I(\omega_i{}^{\perp 2} + \omega_j{}^{\perp 2})/2kT\right). \tag{A 5}$$

It is convenient to introduce new variables x, y and z defined as

$$\left.\begin{aligned} x &\equiv (\mu/2kT)^{1/2} v_{\text{rel}}{}^{\perp}, \\ y &\equiv (I/2kT)^{1/2} \omega_i{}^{\perp}, \\ z &\equiv -(I/2kT^{1/2} \omega_j{}^{\perp} \end{aligned}\right\} \tag{A 6}$$

With these definitions it follows that

$$P(x, y, z) = (\pi)^{-3/2} \exp\left(-(x^2 + y^2 + z^2)\right) \tag{A 7}$$

and

$$(\Delta v_{\text{imp}})_{\perp} = (2kT/\mu)^{1/2} (x + (\mu/I)^{1/2} (\alpha y + \beta z)). \tag{A 8}$$

In order to obtain $\langle (\Delta v_{\text{imp}})_{\perp} \rangle$ we have to average (A 8) over all *positive* values of $(\Delta v_{\text{imp}})_{\perp}$. The condition $(\Delta v_{\text{imp}})_{\perp} > 0$ can be expressed as a vector relation :

$$(\Delta v_{\text{imp}})_{\perp} = \mathbf{r} \,.\, \mathbf{a} > 0, \tag{A 9}$$

where $\mathbf{r} = (x, y, z)$ and $\mathbf{a}$ is a vector with components $((2kT/\mu)^{1/2}$, $\alpha(2kT/I)^{1/2}$, $\beta(2kT/I)^{1/2})$. Introducing θ, the angle between $\mathbf{r}$ and $\mathbf{a}$, we can rewrite (A 9) as

$$(\Delta v_{\text{imp}})_{\perp} = r(2kT/\mu)^{1/2} (1 + (\mu/I)(\alpha^2 + \beta^2))^{1/2} \cos\theta. \tag{A 10}$$

The evaluation of $\langle (\Delta v_{\text{imp}})_{\perp} \rangle$ is now straightforward :

$$\langle (\Delta v_{\text{imp}})_{\perp} \rangle = \pi^{-3/2} (2kT/\mu)^{1/2} (1 + (\mu/I)(\alpha^2 + \beta^2))^{1/2}$$
$$\times 2\pi \int_0^{\infty} dr r^3 \exp\left(-r^2\right) \int_0^{\pi/2} d\theta \sin\theta \cos\theta$$
$$= (kT/2\pi\mu)^{1/2} (1 + (\mu/I)(\alpha^2 + \beta^2))^{1/2}. \tag{A 11}$$

Inserting this expression in (A 2) we obtain

$$\left\langle \frac{dn}{dt} \right\rangle = (\pi\rho/2)(kT/2\pi\mu)^{1/2} \int_{-L/2}^{L/2} d\alpha \int_{-L/2}^{L/2} d\beta (1+(\mu/I)(\alpha^2+\beta^2))^{1/2}. \quad \text{(A 12)}$$

Equation (A 12) can be further simplified by making the transformation $d\alpha\, d\beta \to u\, du\, d\phi$:

$$\left\langle \frac{dn}{dt} \right\rangle = (\pi\rho/2)(kT/2\pi\mu)^{1/2}\, 8 \int_0^{\pi/4} d\phi \int_0^{L/2\cos\phi} du (1+(\mu/I)u^2)^{1/2}\, u$$

$$= 2\pi\rho(kT/2\pi\mu)^{1/2}(2I/3\mu) \int_0^{\pi/4} d\phi \{(1+(\mu L^2/4I\cos^2\phi))^{3/2}-1\}. \quad \text{(A 13)}$$

Introducing the parameter $\tau = (4I/\mu L^2)$ which characterizes the mass distribution in the rod, we can write (A 13) as :

$$\left\langle \frac{dn}{dt} \right\rangle = (\pi\rho L^2/3)(kT/2\pi\mu)^{1/2}\, \tau \int_0^{\pi/4} d\phi \{(1+1/\tau\cos^2\phi)^{3/2}-1\}. \quad \text{(A 14)}$$

In the case that we have studied the mass distribution in the rods is assumed to be uniform which corresponds to $\tau = 2/3$. Hence, the collision frequency should be given by :

$$\left\langle \frac{dn}{dt} \right\rangle = (2\pi^{1/2}/9)\rho^* \int_0^{\pi/4} d\phi \{(1+\tfrac{3}{2}\cos^2\phi)^{3/2}-1\} = 1{\cdot}2376624\rho^*, \quad \text{(A 15)}$$

where we have used reduced units ($L=1$, $kT=1$, $\mu = m/2 = \frac{1}{2}$). Actually, the collision frequency in a finite system of N particles will differ slightly from the value given by (A 15). Three different factors contribute to this N-dependence. The first is the well known correction to the collision frequency due to the fact that we study a microcanonical rather than a canonical ensemble [18]. In our case, this correction is of order $(1+0{\cdot}05/N)$. The second correction is due to fluctuations in the translational and rotational kinetic energy. This correction is always negative (in the present case : $(1-0{\cdot}006/N)$). The third correction is due to the fact that the instantaneous local density will fluctuate around ρ^*. In the absence of density fluctuations, the leading N-dependence of (A 15) would be $(1-1/N)$. Unless N is very small, the effect of density fluctuations is to cancel this N-dependence. As a consequence, density fluctuations do not lead to an additional N-dependence of (A 15). It should be noted, however, that density fluctuations will contribute to the *noise* in the collision frequency. This effect will become more pronounced in cases were density fluctuations decay slowly. For the system sizes that we used in our simulations ($N=100$ and $N=500$), the systematic N-dependent corrections to (A 15) are too small to be observed, hence we shall disregard them in what follows.

Appendix B

In this appendix we derive ' Enskog ' expressions for the autocorrelation functions of the molecular velocity, angular momentum and rotational kinetic energy. In all three cases, the Enksog correlation function is a simple exponential with a decay time chosen such that the initial slopes of the Enskog correlation functions are equal to those of the real correlation functions, Below we show how

these initial slopes can be evaluated *exactly* in three cases of special relevance. We shall compute the initial slope of the velocity ACF

$$1/\tau_{\mathrm{v}} = \lim_{\epsilon \to 0+} -\frac{\langle \mathbf{v}(0) \,.\, \dot{\mathbf{v}}(\epsilon)}{\langle v(0)^2 \rangle}, \tag{B 1}$$

the angular momentum ACF

$$1/\tau_{\mathrm{J}} = \lim_{\epsilon \to 0+} -\frac{\langle \mathbf{J}(0) \,.\, \dot{\mathbf{J}}(\epsilon) \rangle}{\langle J(0)^2 \rangle} \tag{B 2}$$

and of the ACF of the fluctuating part of the rotational kinetic energy

$$1/\tau_{\epsilon} = \lim_{\delta \to 0+} -\frac{\langle (\epsilon_{\mathrm{R}}(0) - \langle \epsilon \rangle) \epsilon_{\mathrm{R}}(\delta) \rangle}{\langle \epsilon^2 \rangle - \langle \dot{\epsilon} \rangle^2}. \tag{B 3}$$

(1) *Velocity autocorrelation function*

The initial slope of the velocity ACF is given by :

$$1/\tau_{\mathrm{v}} = -\langle \mathbf{v}_i(0) \,.\, \Delta \mathbf{v}_i^{(\text{per collision})} \,.\, \Gamma \rangle, \tag{B 4}$$

where Γ is the rate at which molecule i experiences collisions. Before averaging both Δv and Γ depend on the coordinates and momenta of the collision partners. We have added the subscript i to $\mathbf{v}$ and $\Delta \mathbf{v}$ to indicate that we are considering the change in the velocity of particle i. The choice of the dummy index i is, of course, arbitrary ; we might just as well have picked any other particle j. In particular, instead of i we might have chosen its collision partner j. Hence

$$\langle \mathbf{v}_i(0) \,.\, \Delta \mathbf{v}_i \Gamma \rangle = \langle \mathbf{v}_j(0) \,.\, \Delta \mathbf{v}_j \Gamma \rangle. \tag{B 5}$$

However, as $m_i = m_j$, $\Delta \mathbf{v}_i = -\Delta \mathbf{v}_j$ and consequently

$$\langle \mathbf{v}_i(0) \,.\, \Delta \mathbf{v}_i \Gamma \rangle = \tfrac{1}{2} \langle \mathbf{v}_{\mathrm{rel}} \,.\, \Delta \mathbf{v} \Gamma \rangle, \tag{B 6}$$

where $\mathbf{v}_{\mathrm{rel}} = \mathbf{v}_i(0) - \mathbf{v}_j(0)$ and $\Delta \mathbf{v}$ is given by (30) :

$$\Delta \mathbf{v} = (\Delta \mathbf{P}/m) = -\frac{(v_{\mathrm{rel}} + \alpha \omega_i{}^{\perp} - \beta \omega_j{}^{\perp})}{(1 + m(\alpha^2 + \beta^2)/2I)}. \tag{B 7}$$

As in Appendix A, we change to variables x, y and z as defined in (A 6) and (A 9). The expression for $\Delta \mathbf{v}$ then becomes

$$\Delta \mathbf{v} = -(\mathbf{r} \,.\, \mathbf{a})/(1 + (m/2I)(\alpha^2 + \beta^2)). \tag{B 8}$$

Consequently, (B 6) can be rewritten as

$$\tfrac{1}{2} \langle \mathbf{v}_{\mathrm{rel}} \,.\, \Delta \mathbf{v} \Gamma \rangle = -\tfrac{1}{2} (2kT/\mu)^{1/2} \left\langle \frac{x(\mathbf{r} \,.\, \mathbf{a}) \Gamma(\alpha, \beta \,;\, x, y, z)}{(1 + (m/2I)(\alpha^2 + \beta^2))} \right\rangle. \tag{B 9}$$

As before, (B 9) must be averaged over all directions of $\mathbf{r}$ such that $\mathbf{r} \,.\, \mathbf{a} > 0$. It follows from (A 2) and (A 9) that the collision rate due to collisions with impact distances within a range $d\alpha$ ($d\beta$) around α (β) is given by

$$\Gamma(\alpha, \beta \,;\, x, y, z) = \tfrac{1}{2} \pi \rho (\mathbf{r} \,.\, \mathbf{a}) \, d\alpha \, d\beta. \tag{B 10}$$

Inserting (B 10) in (B 9) we obtain

$$\langle \mathbf{v}(0) \cdot \dot{\mathbf{v}}(0+) \rangle = -\tfrac{1}{2}(2kT/\mu)^{1/2} \frac{\pi\rho}{2} \pi^{-3/2} \int_{-L/2}^{L/2} d\alpha \int_{-L/2}^{L/2} d\beta \int_0^{\infty} dr r^2 \times \int_0^{\pi/2} d\Theta \sin\Theta \int_0^{2\pi} d\phi \left\{ \frac{x r^2 a^2 \cos^2\Theta}{1+(m/2I)(\alpha^2+\beta^2)} \right\} \exp(-r^2), \quad \text{(B 11)}$$

where Θ is the angle between $\mathbf{r}$ and $\mathbf{a}$. The x component of $\mathbf{r}$ may be decomposed into components parallel and perpendicular to $\mathbf{a}$:

$$x = (\mathbf{r} \cdot \mathbf{1}_x) = (\mathbf{r} \cdot \mathbf{1}_a)(\mathbf{1}_a \cdot \mathbf{1}_x) + (\mathbf{r} \cdot \mathbf{1}_b)(\mathbf{1}_b \cdot \mathbf{1}_x) + (\mathbf{r} \cdot \mathbf{1}_c)(\mathbf{1}_c \cdot \mathbf{1}_x), \quad \text{(B 12)}$$

where $\mathbf{1}_a$ is a unit vector parallel to $\mathbf{a}$, $\mathbf{1}_c$ is perpendicular to both $\mathbf{a}$ and $\mathbf{1}_x$, and $\mathbf{1}_b$ is perpendicular to both $\mathbf{1}_a$ and $\mathbf{1}_c$. As $\mathbf{1}_c \cdot \mathbf{1}_x = 0$, the third term on the right hand side of (B 12) vanishes. The second term,

$$(\mathbf{r} \cdot \mathbf{1}_b)(\mathbf{1}_b \cdot \mathbf{1}_x) = r \sin\Theta \cos\phi (\mathbf{1}_b \cdot \mathbf{1}_x),$$

yields zero upon integration over ϕ in (B 11). Hence only the first term in (B 12) remains, and we obtain the following expression for (B 11):

$$\langle \mathbf{v}(0) \cdot \dot{\mathbf{v}}(0+) \rangle = -\tfrac{1}{2} \left(\frac{2kT}{\mu} \right)^{1/2} \frac{\pi\rho}{2} \pi^{-3/2} \int_{-L/2}^{L/2} d\alpha \int_{-L/2}^{L/2} d\beta \int_0^{\infty} dr \int_0^1 d\cos\Theta \frac{2\pi r^5 \cos^3\Theta a^2 (\mathbf{1}_a \cdot \mathbf{1}_x)}{(1+(m/2I)(\alpha^2+\beta^2))} \exp(-r^2). \quad \text{(B 13)}$$

It should be noted that $\mathbf{1}_a \cdot \mathbf{1}_x = (2kT/\mu)^{1/2}/((2kT/\mu)(1+(m/2I)(\alpha^2+\beta^2)^{1/2})$ is independent of r, Θ and ϕ. The integrals over r and Θ in (B 13) are elementary and yield

$$\langle \mathbf{v}(0) \cdot \dot{\mathbf{v}}(0+) \rangle = -\frac{\rho\pi^{1/2}}{8} \left(\frac{2kT}{\mu} \right)^{3/2} \int_{-L/2}^{L/2} d\alpha \int_{-L/2}^{L/2} d\beta (1+(m/2I)(\alpha^2+\beta^2))^{-1/2}. \quad \text{(B 14)}$$

As before (see (A 13)) we transform from the variables α and β to u and ϕ. After integrating over u the final expression for $\langle \mathbf{v}(0) \cdot \dot{\mathbf{v}}(0+) \rangle$ becomes

$$\langle \mathbf{v}(0) \cdot \dot{\mathbf{v}}(0+) \rangle = -\rho\pi^{1/2}(2kT/\mu) t^{3/2} \frac{2I}{m} \int_0^{\pi/4} \{(1+mL^2/8I\cos^2\phi)^{1/2} - 1\} d\phi \quad \text{(B 15)}$$

or in reduced units ($L=1$, $kT=1$, $m=1$):

$$\langle \mathbf{v}(0) \cdot \dot{\mathbf{v}}(0+) \rangle = -2\pi^{1/2} \rho^* \tau \int_0^{\pi/4} \{(1+1/\tau\cos^2\phi)^{1/2} - 1\} d\phi, \quad \text{(B 16)}$$

where $\tau = 8I/mL^2$. For uniform rods $\tau = 2/3$. Performing the integral in (B 16) for this value of τ, we obtain

$$\langle \mathbf{v}(0) \cdot \dot{\mathbf{v}}(0+) \rangle = -1{\cdot}3024830\rho^*, \quad \text{(B 17)}$$

and therefore $1/\tau_v$ as defined in (B 1) is given by

$$1/\tau_v = 0{\cdot}4341610\rho^*. \quad \text{(B 18)}$$

As the self diffusion constant is related to the velocity ACF by

$$D=(1/3)\int_0^\infty \langle \mathbf{v}(0)\,.\,\mathbf{v}(t)\rangle\, dt, \tag{B 19}$$

we find that the Enskog approximation for D is

$$D^{\mathrm{E}}=2{\cdot}303293/\rho^*. \tag{B 20}$$

(2) *Angular momentum autocorrelation function*

The procedure to obtain the angular momentum ACF in the Enskog approximation is quite similar to the one used to derive the velocity ACF. We shall therefore limit ourselves to a rather compact derivation. Below we use the same notation as was used in the previous section. According to (B 2) we need to evaluate

$$\lim_{\epsilon\to 0+}\langle \mathbf{J}(0)\,.\,\dot{\mathbf{J}}(\epsilon)\rangle=\langle \mathbf{J}_i(0)\,.\,\Delta\mathbf{J}_i\Gamma(\alpha,\beta\,;\;x,y,z)\rangle. \tag{B 21}$$

As

$$\mathbf{J}_i\,.\,\Delta\mathbf{J}_i=\mathbf{J}_i\,.\,\alpha\mathbf{u}_i\wedge\Delta\mathbf{P}_i, \tag{B 22}$$

we need only consider the component of $\mathbf{J}_i$ that is perpendicular to the transferred momentum $\Delta\mathbf{P}$, i.e.

$$\mathbf{J}_i\,.\,\Delta\mathbf{J}_i=\alpha I\omega_i^{\perp}\,\Delta P \tag{B 23}$$

(see (A 4)). Using the same notation as in (B 11) we may rewrite (B 21) as

$$\langle \mathbf{J}(0)\,.\,\dot{\mathbf{J}}(0+)\rangle=-\frac{I\pi\rho}{2}\int_{-L/2}^{L/2}d\alpha\int_{-L/2}^{L/2}d\beta\pi^{-3/2}\int_0^\infty drr^2\int_0^1 d\cos\Theta\int_0^{2\pi}d\phi \times\left[\frac{\alpha(2kT/I)^{1/2}\,ymr^2\,a^2\cos\Theta}{(1+(m/2I)(\alpha^2+\beta^2))}\right]\exp(-r^2). \tag{B 24}$$

Performing the integrals over r, Θ and ϕ we obtain

$$\langle \mathbf{J}(0)\,.\,\dot{\mathbf{J}}(0+)\rangle=-\frac{\pi^{1/2}\rho}{8}\left(\frac{2kT}{\mu}\right)^{3/2}m^3\int_{-L/2}^{L/2}d\alpha\int_{-L/2}^{L/2}d\beta\alpha^2(1+(m/2I)(\alpha^2+\beta^2))^{-1/2}. \tag{B 25}$$

As before we transform from the variables α, β to u, ϕ. Making use of the fact that α and β are interchangeable (B 25) can be rewritten as :

$$\langle \mathbf{J}(0)\,.\,\dot{\mathbf{J}}(0+)\rangle=-\frac{\pi^{1/2}\rho L^2}{4}\left(\frac{2kT}{\mu}\right)^{1/2}(2IkT)\tau \times\int_0^{\pi/4}\left[\frac{2(1+1/\tau\cos^2\phi)^{1/2}}{\tau\cos^2\phi}-\tfrac{4}{3}(1+1/\tau\cos^2\phi)^{3/2}+\tfrac{4}{3}\right]d\phi. \tag{B 26}$$

Hence the following expression results for $1/\tau_{\mathrm{J}}$ (B 2) :

$$1/\tau_{\mathrm{J}}=\frac{\pi^{1/2}}{2}\rho^*\tau\int_0^{\pi/4}\left[\frac{2(1+1/\tau\cos^2\phi)^{1/2}}{\tau\cos^2\phi}-\tfrac{4}{3}(1+1/\tau\cos^2\phi)^{3/2}+\tfrac{4}{3}\right]d\phi. \tag{B 27}$$

In particular for $\tau(=8I/mL^2)=\frac{2}{3}$:

$$1/\tau_{\mathrm{J}}=0{\cdot}5864209\rho^* \tag{B 28}$$

or

$$\tau_J = 1{\cdot}70526/\rho^*. \tag{B 29}$$

(3) *Rotational energy autocorrelation function*

The derivation of the Enskog expressions for the rotational energy ACF follows the same steps as the ones presented above. The actual evaluation is, however, somewhat more tedious and we will therefore only quote the results. $1/\tau_\epsilon$ is defined in (B 3):

$$1/\tau_\epsilon = \lim_{\delta \to 0+} \frac{\langle (\epsilon_R(0) - \langle \epsilon_R \rangle)\epsilon_R(\delta) \rangle}{\langle \epsilon_R{}^2 - \langle \epsilon_R \rangle^2}, \tag{B 3}$$

where $\epsilon_R = J^2/2I$ and

$$\langle \epsilon_R \rangle = kT. \tag{B 30}$$

We obtain the following relation between τ_ϵ and the density ρ^*:

$$1/\tau_\epsilon = \pi^{1/2}\rho^*\tau \int_0^{\pi/4} \Bigg[(\cos^4\phi + \sin^4\phi) \left\{ \frac{2(1+1/\tau\cos^2\phi)^{-1/2}}{\tau^2\cos^4\phi} - \frac{8(1+1/\tau\cos^2\phi)^{1/2}}{\tau\cos^2\phi} + \tfrac{16}{3}(1+1/\tau\cos^2\phi)^{3/2} - \tfrac{16}{3} \right\} + \left\{ \frac{2}{\tau\cos^2\phi}(1+1/\tau\cos^2\phi)^{1/2} - \tfrac{4}{3}(1+1/\tau\cos^2\phi)^{3/2} + \tfrac{4}{3} \right\} \Bigg] d\phi, \tag{B 31}$$

where, as before, $\tau = 8I/mL^2$. For uniform rods ($\tau = \frac{2}{3}$)

$$1/\tau_\epsilon = 0{\cdot}7486168\rho^* \tag{B 32}$$

or

$$\tau_\epsilon = 1{\cdot}335767/\rho^*. \tag{B 33}$$

References

[1] Alder, B. J., and Wainwright, T. E., 1970, *Phys. Rev.* A, **1,** 18.
[2] Barker, J. A., and Henderson, D., 1967, *J. chem. Phys.*, **47,** 4714.
[3] Weeks, J. D., Chandler, D., and Andersen, H. C., 1971, *J. chem. Phys.*, **54,** 5237.
[4] de Gennes, P. G., 1974, *The Physics of Liquid Crystals* (Oxford University Press).
[5] Frenkel, D., and Eppenga, R., 1982, *Phys. Rev. Lett.*, **49,** 1089.
[6] Frenkel, D., and Eppenga, R. (to be published).
[7] Maguire, J. F., McTague, J. P., and Rondelez, F., 1980, *Phys. Rev. Lett.*, **45,** 1891.
[8] Maguire, J. F., 1981, *J. chem. Soc. Faraday Trans. II,* **77,** 513.
[9] Zero, K. M., and Pecora, R., 1982, *Macromolecules,* **15,** 87.
[10] Doi, M., 1975, *J. Phys., Paris,* **36,** 607.
[11] Doi, M., and Edwards, S. F., 1978, *J. chem. Soc. Faraday Trans. II,* **74,** 560.
[12] Frenkel, D., and Maguire, J. F., 1981, *Phys. Rev. Lett.*, **47,** 1025.
[13] Rebertus, D. W., and Sando, K. M., 1977, *J. chem. Phys.*, **67,** 2585.
[14] Bellemans, A., Orban, J., and van Belle, D., 1980, *Molec. Phys.*, **39,** 781.
[15] Stratt, R. M., Holmgren, S. L., and Chandler, D., 1981, *Molec. Phys.*, **42,** 1233.
[16] McNeill, W. J., and Madden, W. G., 1982, *J. chem. Phys.*, **76,** 6221.
[17] Alder, B. J., and Wainwright, T. E., 1959, *J. chem. Phys.*, **31,** 549.
[18] Erpenbeck, J. J., and Wood, W. W., 1977, *Statistical Mechanics :* Part B, *Time Dependent Processes,* edited by B. J. Berne (Plenum).
[19] O'Dell, J., and Berne, B. J., 1975, *J. chem. Phys.*, **63,** 2376.
[20] Berne, B. J., 1977, *J. chem. Phys.*, **66,** 2821.

[21] PANGALI, C. S., and BERNE, B. J., 1977, *J. chem. Phys.*, **67,** 4571.
[22] CHANDLER, D., 1974, *J. chem. Phys.*, **60,** 3500.
[23] CHANDLER, D., 1974, *J. chem. Phys.*, **60,** 3508.
[24] GORDON, R. G., 1966, *J. chem. Phys.*, **44,** 1830.
[25] STEELE, W. A., 1976, *Adv. chem. Phys.*, **34,** 1.
[26] FRENKEL, D., and WEGDAM, G. H., 1974, *J. chem. Phys.*, **61,** 4671. FRENKEL, D., 1977, Thesis, Amsterdam.
[27] HUBBARD, P. S., 1963, *Phys. Rev.*, **131,** 1155.
[28] DE GENNES, P. G. 1979, *Scaling Concepts in Polymer Physics* (Cornell University Press).
[29] FEYNMAN, R. P., and HIBBS, A. R., 1965, *Quantum Mechanics and Path Integrals* (McGraw-Hill).
[30] ZIMAN, J. M., 1979, *Models of Disorder* (Cambridge U.P.).
[31] ZWANZIG, R., and AILAWADI, N. K., 1969, *Phys. Rev.*, **182,** 280.
[32] FRENKEL, D., 1980, *Intermolecular Spectroscopy and Dynamical Properties of Dense Systems* (Proceedings of the International School of Physics 'Enrico Fermi', Vol. LXXV) (Soc. Italiana di Fisica).
[33] KEYES, T., and KIVELSON, D., 1972, *J. chem. Phys.*, **56,** 1057.
[34] BERNE, B. J., and PECORA, R., 1976, *Dynamic Light Scattering* (John Wiley & Sons).
[35] For a detailed review, see : KIVELSON, D., and MADDEN, P., 1980, *A. Rev. phys. Chem.*, **31,** 523.